



Particles on demand method: Theoretical analysis, simplification techniques, and model extensionsN. G. Kallikounis and I. V. Karlin ^{*}*Department of Mechanical and Process Engineering, ETH Zurich, 8092 Zurich, Switzerland* (Received 31 January 2023; revised 24 May 2023; accepted 22 November 2023; published 22 January 2024)

The particles on demand method [Phys. Rev. Lett. **121**, 130602 (2018)] was recently formulated with a conservative finite-volume discretization and validated against challenging benchmarks. In this work, we focus on the properties of the reference frame transformation and its implications on the accuracy of the model. Based on these considerations, we propose strategies that simplify the scheme and generalize it to include a tunable Prandtl number via quasi-equilibrium relaxation. Finally, we adapt concepts from the multiscale semi-Lagrangian lattice Boltzmann formulation to the proposed framework, further improving the potential and the operating range of the kinetic model. Numerical simulations of high Mach compressible flows demonstrate excellent accuracy and stability of the model over a wide range of conditions.

DOI: [10.1103/PhysRevE.109.015304](https://doi.org/10.1103/PhysRevE.109.015304)**I. INTRODUCTION**

Understanding of the nature of high-speed compressible flows has been a long sought goal in the scientific and engineering communities. Accurate prediction of complex hydrodynamic features is crucial in modern research, as well as in technology, with examples such as the interpretation of astrophysical jets, captured in the images of deep space telescopes [1,2] and the design of air frames and propulsion systems of high-Mach low-altitude flying vehicles [3]. Throughout the history of computational fluid dynamics (CFD), a number of numerical approaches has been suggested for the simulation of high-speed flows, including artificial viscosity methods [4], total variation diminishing (TVD) [5], essentially nonoscillatory (ENO) schemes [6,7] and weighted ENO (WENO) schemes [8,9]. The challenging nature of these flows renders the field an active research area [10,11], with developments such as positivity-preserving limiters and targeted ENO (TENO) schemes [12] extending the domain of CFD towards even more exotic hydrodynamics [13–15].

In contrast with conventional CFD, the lattice Boltzmann method (LBM) addresses the evolution of hydrodynamic fields through the dynamics of a fully discrete kinetic system of designed particles associated with the discrete velocities c_i , $i = 0, \dots, Q - 1$. The state is described in terms of the populations $f_i(\mathbf{x}, t)$, which evolve in time and space by a simple algorithm “stream along links c_i and collide at the nodes \mathbf{x} in discrete time t .” LBM has evolved into a versatile tool for the simulation of complex flows including transitional flows [16], flows in complex moving geometries [17],

thermal and convective flows [18–20], multiphase and multicomponent flows [21–24], reactive flows [25], and rarefied gas [26], to mention a few recent instances; see Refs. [27–29] for a discussion of LBM and its application areas. However, despite the high efficiency and low numerical dissipation of LBM for nearly incompressible flows, the domain of high-speed compressible flows presents a number of severe challenges [18,19,30–32]. The main directions to extend conventional LBM towards the compressible realm includes standard LBM augmented with correction terms [33–36], multispeed lattices [37–41], and hybrid approaches [42–45].

A common feature of the conventional LBM is the propagation of the populations with fixed discrete velocities, which translates as fixing the reference frame “at rest.” It is well known that, when the fluid velocity significantly deviates from the frame velocity, errors and numerical instabilities corrupt the solution, impeding the applicability of LBM to high-Mach flows [30,33,46]. A remedy was the introduction of *uniformly* shifted lattices, which amounts to a constant shift of the reference frame, at every grid point of the numerical domain [47]. The concept demonstrated excellent performance for predominately unidirectional compressible flows, shifting the operational domain of the method in par with the chosen reference velocity shift [34,41,47]. While the concept of the uniform frame shift maintains key advantages of the scheme, such as simplicity and exact propagation, its potential diminishes for flows exhibiting large variations in flow velocity and temperature due to the inevitable presence of strong deviations between the velocity of the actual flow and the imposed reference frame.

In contrast with the conventional LBM, the recently proposed particles on demand (PonD) method reformulates the kinetic equations in a space-time adaptive reference frame, dictated by the actual local fluid velocity and temperature [48]. Two key elements were introduced with the PonD method: First, PonD uses a consistent representation of populations in different reference frames, an operation termed as reference frame transformation. Second, a predictor-corrector

^{*}Corresponding author: ikarlin@ethz.ch

iteration loop was applied, which ensured the realization of the propagation and collision step in the local comoving reference frame, thereby optimizing accuracy and stability. Early realizations of PonD employed a semi-Lagrangian discretization, providing off-lattice flexibility to accommodate a varying reference frame, and validated the central concepts with a series of benchmarks, including multiphase and rarefied flows [49–55]. However, the semi-Lagrangian method is prone to errors in conservation of mass, momentum, and energy, deteriorating the accuracy of the solution in the presence of discontinuities (shock waves) [56]. As a remedy to these shortcomings, a finite-volume formulation of PonD was proposed in Ref. [56], following the discrete unified gas kinetic scheme (DUGKS) [57–59]. The resulting conservative scheme, combined with a reference frame transformation based on Grad’s projection of populations, demonstrated excellent performance in an array of challenging hypersonic compressible benchmark flows, including extreme hydrodynamic features such as the formation of near-vacuum regions. It is worth noting earlier approaches with adaptive particles velocities, e.g., a finite-volume solver for the Euler equations suggested by Nadiga [60] and an adaptive LBM model by Sun [61]. In these works, no reference frame transformation is involved, which constitutes a major limitation as compared with PonD. In particular, the model of Sun [61] is designed for a fixed relaxation time equal to one.

In this paper, we aim at a further development of the finite-volume formulation of PonD, targeting strategies that simplify the scheme. The implications of the reference frame transformation and the frame invariant moments are the primary focus of this work. The scheme is extended to include a forcing term, as well as a variable Prandtl number. Finally, we combine the idea of the multiscale framework suggested in Ref. [53] with Grad’s projection frame transformation. The theoretical findings are validated in a series of numerical experiments along with extensive benchmarking of the scheme in challenging hydrodynamic flows.

The paper is organized as follows: The formulation of the kinetic equations in an adaptive reference frame is laid out in Sec. II. Section III presents the kinetic model, which allows for variable adiabatic exponent and Prandtl number. Subsequently, Sec. IV describes the numerical discretization of the model. The model is extensively benchmarked in Sec. V, along with a demonstration of importance of the reference frame transformation. Finally, concluding remarks are provided in Sec. VI.

II. ADAPTIVE REFERENCE FRAME FORMULATION

A. Discrete velocities

Without loss of generality, we consider discrete speeds in two dimensions formed by tensor products of roots of Hermite polynomials $c_{i\alpha}$,

$$\mathbf{c}_i = (c_{ix}, c_{iy}). \quad (1)$$

The model is characterized by the lattice temperature T_L and the weights W_i associated with the vectors (1),

$$W_i = w_{ix}w_{iy}, \quad (2)$$

where $w_{i\alpha}$ are weights of the Gauss–Hermite quadrature [26]. The discrete speeds and the associated weights are shown in

TABLE I. Lattice temperature T_L , roots of Hermite polynomials $c_{i\alpha}$ and weights $w_{i\alpha}$ of the $D = 1$ Gauss–Hermite quadrature, and nomenclature.

Model	T_L	$c_{i\alpha}$	$w_{i\alpha}$	$D = 2$
D1Q3	1	0	2/3	D2Q9
		$\pm\sqrt{3}$	1/6	
D1Q4	1	$\pm\sqrt{3 - \sqrt{6}}$	$(3 + \sqrt{6})/12$	D2Q16
		$\pm\sqrt{3 + \sqrt{6}}$	$(3 - \sqrt{6})/12$	
D1Q5	1	0	8/15	D2Q25
		$\pm\sqrt{5 - \sqrt{10}}$	$(7 + 2\sqrt{10})/60$	
		$\pm\sqrt{5 + \sqrt{10}}$	$(7 - 2\sqrt{10})/60$	

Table I. With the discrete speeds (1), the particles’ velocities $\mathbf{v}_i^{\lambda_{\text{ref}}}$ are defined relative to a reference frame λ_{ref} , specified by the frame velocity \mathbf{u}_{ref} and the frame temperature T_{ref} ,

$$\lambda_{\text{ref}} = \{\mathbf{u}_{\text{ref}}, T_{\text{ref}}\}, \quad (3)$$

$$\mathbf{v}_i^{\lambda_{\text{ref}}} = \sqrt{\frac{T_{\text{ref}}}{T_L}} \mathbf{c}_i + \mathbf{u}_{\text{ref}}. \quad (4)$$

The optimal reference frame is the comoving reference frame, which is specified by the *local* temperature $T_{\text{ref}} = T(\mathbf{x}, t)$ and the *local* flow velocity $\mathbf{u}_{\text{ref}} = \mathbf{u}(\mathbf{x}, t)$.

B. Reference frame transformation

A critical element of our construction is the transformation of the populations f_i^λ , defined with respect to a λ reference frame, to a different reference frame λ' ,

$$\lambda' = \{\mathbf{u}', T'\}. \quad (5)$$

In this work, we follow the strategy of Ref. [56]. Let us denote \mathbf{M}_k^λ a moment tensor of order k ,

$$\mathbf{M}_k^\lambda = \sum_{i=0}^{Q-1} f_i^\lambda \underbrace{\mathbf{v}_i^\lambda \mathbf{v}_i^\lambda \cdots \mathbf{v}_i^\lambda}_k. \quad (6)$$

The reference frame transformation is then defined by the condition of invariance of the moments of orders $k = 0, 1, \dots, K$,

$$\mathbf{M}_k^{\lambda'} = \mathbf{M}_k^\lambda, \quad k = 0, 1, \dots, K, \quad (7)$$

where K denotes the maximal moment order which is required to be frame invariant. The transformed populations are then sought as a Grad projection,

$$f_i^{\lambda'} = W_i \sum_{n=0}^K \frac{1}{n!} \boldsymbol{\alpha}^{(n)}(\mathbf{m}; \lambda') : \mathbf{H}^{(n)}(\mathbf{c}_i), \quad (8)$$

where $\mathbf{H}^{(n)}(\mathbf{c}_i)$ correspond to the Hermite polynomials of the lattice speeds and the expansion coefficients $\boldsymbol{\alpha}^{(n)}(\mathbf{m}; \lambda')$ are calculated such that the moment invariant system (7) is satisfied (detailed in Appendix A). The latter depend on the vector of frame invariant moments $\mathbf{m} = \{\mathbf{M}_0, \dots, \mathbf{M}_K\}$ and the target reference frame λ' . As a shorthand notation for the reference frame transformation, we use the following formula:

$$f_i^{\lambda'} = \mathcal{G}_{i,\lambda}^{\lambda'} f_i^\lambda. \quad (9)$$

C. Solution methodology

To illustrate the solution methodology of PonD, we consider a domain with N grid points with the following initial conditions,

$$f_i^{\lambda(x_j)}(\mathbf{x}_j, t_0), \quad j = 1, \dots, N. \quad (10)$$

To simplify the notation, we drop the spatial dependence of the reference frame and λ is reserved for the local reference frame, $\lambda = \lambda(\mathbf{x})$. The objective is to solve the kinetic equations with an adaptive reference frame; the populations at the grid point \mathbf{x}_j shall be updated in a reference frame $\bar{\lambda}_j$. The idea of PonD is the following: instead of solving one governing kinetic equation over the numerical domain, we formulate N different problems, each of which solves the kinetic equation in a *uniform* reference frame. To accomplish this strategy, we first need to formulate the proper initial conditions. This is performed through the reference frame transformation. We end up with a list of frame copies,

$$\text{Frame 1 : } \mathcal{G}_{i,\lambda}^{\bar{\lambda}_1} f^\lambda(\mathbf{x}_j, t_0), \quad j = 1, \dots, N, \quad (11)$$

$$\text{Frame 2 : } \mathcal{G}_{i,\lambda}^{\bar{\lambda}_2} f^\lambda(\mathbf{x}_j, t_0), \quad j = 1, \dots, N, \quad (12)$$

⋮

$$\text{Frame } N : \mathcal{G}_{i,\lambda}^{\bar{\lambda}_N} f^\lambda(\mathbf{x}_j, t_0), \quad j = 1, \dots, N. \quad (13)$$

All frame copies are subsequently updated from time t_0 to $t_0 + \delta t$. Each grid point has multiple solutions which correspond to the different reference frame realizations. We keep the solution in which the local reference frame is used: at the point \mathbf{x}_j we keep the solution from the $\bar{\lambda}_j$ frame copy. Using a semi-Lagrangian discretization scheme, the solution at $(\mathbf{x}_j, t_0 + \delta t)$ in the $\bar{\lambda}_j$ frame copy is

$$\mathcal{G}_{i,\lambda}^{\bar{\lambda}_j} f^\lambda(\mathbf{x}_j, t_0 + \delta t) = \mathcal{G}_{i,\lambda}^{\bar{\lambda}_j} f^\lambda(\mathbf{x}_j - \mathbf{v}_i^{\bar{\lambda}_j} \delta t, t_0) + \mathcal{G}_{i,\lambda}^{\bar{\lambda}_j} \Omega(\mathbf{x}_j, t_0), \quad (14)$$

where Ω stands for the collision operator. The populations can be approximated around (\mathbf{x}_j, t_0) with a Taylor expansion:

$$\begin{aligned} \mathcal{G}_{i,\lambda}^{\bar{\lambda}_j} f^\lambda(\mathbf{x}_j - \mathbf{v}_i^{\bar{\lambda}_j} \delta t, t) &= \mathcal{G}_{i,\lambda}^{\bar{\lambda}_j} f^\lambda(\mathbf{x}_j, t) \\ &- \mathbf{v}_i^{\bar{\lambda}_j} \delta t \cdot \nabla (\mathcal{G}_{i,\lambda}^{\bar{\lambda}_j} f^\lambda)(\mathbf{x}_j, t) + O(\delta t^2). \end{aligned} \quad (15)$$

At this point we stress the importance of our effort into generating a list of frame copies. In each of these copies, the reference frame, and therefore the discrete particle velocities, are uniform. Thus, the velocities $\mathbf{v}_i^{\bar{\lambda}_j}$ commute with the spatial derivatives. Treating similarly the temporal derivative and omitting terms of $O(\delta t^2)$ recovers the following equation:

$$\partial_t (\mathcal{G}_{i,\lambda}^{\bar{\lambda}_j} f^\lambda) + \mathbf{v}_i^{\bar{\lambda}_j} \cdot \nabla (\mathcal{G}_{i,\lambda}^{\bar{\lambda}_j} f^\lambda) = \mathcal{G}_{i,\lambda}^{\bar{\lambda}_j} \Omega_f^\lambda. \quad (16)$$

We emphasize that the kinetic equation (16) is formulated with respect to a uniform frame $\bar{\lambda}$. Therefore, Eq. (16) constitutes a typical kinetic equation, with constant characteristics, amenable to usual numerical realizations in the context of LBM, such as integration along characteristics. The necessary element is the introduction of the frame transformation operator. The effect of the varying reference frame is evident in the operation $\mathcal{G}_{i,\lambda}^{\bar{\lambda}_j} f^\lambda$, inside the nonlocal gradient operations. The above observation is crucial and determines the requirements that must be satisfied by the reference frame transformation.

Comments are in order:

(1) The kinetic equations can be formulated in principle with respect to any arbitrary reference frame. As such, different monitoring points can employ different reference frames. The consistency of the evolution in different reference frames is established by proper reference frame transformations. In the limit of infinite discrete velocities, the solution in every frame would be identical, i.e., no reason to do that. But in discrete systems, the accuracy of the solution depends on the proximity of the imposed frame with the actual local frame, dictated by the local flow conditions. Thus, with this procedure, we maximize the accuracy of a given model across the domain.

(2) The direct formulation of a kinetic equation with adaptive velocities leads to additional “forcing” terms, containing derivatives of the particles speeds. A thorough discussion in this direction can be found in Ref. [62]. In the context of PonD, the solution methodology consists of a set of equations, each one at its own, spatially uniform, reference frame. This strategy avoids the explicit requirement for the computation of forcing terms. The price to be paid instead amounts to the operation of reference frame transformations.

(3) Which domain needs to be transformed around a “frame-generating” monitoring point? Thanks to the hyperbolicity of the system, only the numerical domain of dependence needs to be transformed. Of course, this procedure for elliptic type of equations would be prohibitively computationally demanding.

The discussion is continued in Sec. VA via the aid of numerical simulations.

D. Hydrodynamic limit analysis

We analyze the governing kinetic equation (16) with the Chapman–Enskog method and investigate the consistency requirements for the moment invariant system. We rewrite Eq. (16) in terms of a Bhatnagar–Gross–Krook (BGK) collision operator and a small parameter ϵ for the relaxation time τ_1 ,

$$\partial_t (\mathcal{G}_{i,\lambda}^{\bar{\lambda}_j} f^\lambda) + \mathbf{v}_i^{\bar{\lambda}_j} \cdot \nabla (\mathcal{G}_{i,\lambda}^{\bar{\lambda}_j} f^\lambda) = \frac{1}{\epsilon \tau_1} \mathcal{G}_{i,\lambda}^{\bar{\lambda}_j} (f^{\lambda,\text{eq}} - f^\lambda). \quad (17)$$

Following the conventional notation, we introduce the following multiscale expansion:

$$\partial_t = \partial_t^{(1)} + \epsilon \partial_t^{(2)} + O(\epsilon^2), \quad (18)$$

$$f_i^\lambda = f_i^{\lambda,(0)} + \epsilon f_i^{\lambda,(1)} + \epsilon^2 f_i^{\lambda,(2)} + O(\epsilon^3). \quad (19)$$

We inject the expansions into the governing equations and separate the dynamics according to different orders of ϵ ,

$$O(\epsilon^0) : \quad \mathcal{G}_{i,\lambda}^{\bar{\lambda}_j} f_i^{\lambda,(0)} = \mathcal{G}_{i,\lambda}^{\bar{\lambda}_j} f_i^{\lambda,\text{eq}}, \quad (20)$$

$$\begin{aligned} O(\epsilon^1) : \quad & \partial_t^{(1)} (\mathcal{G}_{i,\lambda}^{\bar{\lambda}_j} f_i^{\lambda,(0)}) + \mathbf{v}_i^{\bar{\lambda}_j} \cdot \nabla (\mathcal{G}_{i,\lambda}^{\bar{\lambda}_j} f_i^{\lambda,(0)}) \\ &= -\frac{1}{\tau_1} \mathcal{G}_{i,\lambda}^{\bar{\lambda}_j} f_i^{\lambda,(1)}, \end{aligned} \quad (21)$$

$$\begin{aligned} O(\epsilon^2) : \quad & \partial_t^{(2)} (\mathcal{G}_{i,\lambda}^{\bar{\lambda}_j} f_i^{\lambda,(0)}) + \partial_t^{(1)} (\mathcal{G}_{i,\lambda}^{\bar{\lambda}_j} f_i^{\lambda,(1)}) \\ &+ \mathbf{v}_i^{\bar{\lambda}_j} \cdot \nabla (\mathcal{G}_{i,\lambda}^{\bar{\lambda}_j} f_i^{\lambda,(1)}) = -\frac{1}{\tau_1} \mathcal{G}_{i,\lambda}^{\bar{\lambda}_j} f_i^{\lambda,(2)}. \end{aligned} \quad (22)$$

At the $O(\epsilon^0)$ order we obtain the equilibrium populations,

$$\mathcal{G}_{i,\lambda}^{\bar{\lambda}} f^{\lambda,(0)} = \mathcal{G}_{i,\lambda}^{\bar{\lambda}} f^{\lambda,\text{eq}} \Leftrightarrow f_i^{\lambda,(0)} = f_i^{\lambda,\text{eq}}, \quad (23)$$

which implies the following solvability constraints,

$$\sum_{i=0}^{Q-1} \{1, \mathbf{v}_i^{\bar{\lambda}}, (v_i^{\bar{\lambda}})^2\} \mathcal{G}_{i,\lambda}^{\bar{\lambda}} f^{\lambda,(k)} = \{0, \mathbf{0}, 0\}, \quad k \geq 1. \quad (24)$$

1. Equilibrium moments

The functional form of the equilibrium moments is the basic element of the analysis and determines the recovered hydrodynamic equations. We underline that all the lattices discussed in this work and listed in Table I, reproduce the pertinent equilibrium moments as their Maxwell–Boltzmann (MB) continuous counterparts in the comoving reference frame. For example, even for the standard $D2Q9$ lattice, the evaluation with the comoving reference frame

$$\lambda = \{\mathbf{u}, T\}, \quad (25)$$

$$\mathbf{v}_i^{\lambda} = \sqrt{T/T_L} \mathbf{c}_i + \mathbf{u}, \quad (26)$$

$$f_i^{\text{eq},\lambda} = \rho W_i \quad (27)$$

retrieves the following moments:

$$\mathbf{J}^{\text{eq},\lambda} = \sum_{i=0}^{Q-1} \mathbf{v}_i^{\lambda} f_i^{\text{eq},\lambda} = \mathbf{J}^{\text{MB}}, \quad (28)$$

$$\mathbf{P}^{\text{eq},\lambda} = \sum_{i=0}^{Q-1} v_i^{\lambda} \mathbf{v}_i^{\lambda} f_i^{\text{eq},\lambda} = \mathbf{P}^{\text{MB}}, \quad (29)$$

$$\mathbf{Q}^{\text{eq},\lambda} = \sum_{i=0}^{Q-1} v_i^{\lambda} \mathbf{v}_i^{\lambda} v_i^{\lambda} f_i^{\text{eq},\lambda} = \mathbf{Q}^{\text{MB}}, \quad (30)$$

$$\mathbf{q}^{\text{eq},\lambda} = \sum_{i=0}^{Q-1} v_i^{\lambda} (v_i^{\lambda})^2 f_i^{\text{eq},\lambda} = \mathbf{q}^{\text{MB}}, \quad (31)$$

$$\mathbf{R}^{\text{eq},\lambda} = \sum_{i=0}^{Q-1} (v_i^{\lambda})^2 \mathbf{v}_i^{\lambda} v_i^{\lambda} f_i^{\text{eq},\lambda} = \mathbf{R}^{\text{MB}}, \quad (32)$$

where the MB moments are

$$\mathbf{J}^{\text{MB}} = \rho \mathbf{u}, \quad (33)$$

$$\mathbf{P}^{\text{MB}} = \rho T \mathbf{I} + \rho \mathbf{u} \mathbf{u}, \quad (34)$$

$$\mathbf{Q}^{\text{MB}} = \rho T \overline{\mathbf{u} \mathbf{u}} + \rho \mathbf{u} \mathbf{u} \mathbf{u}, \quad (35)$$

$$\mathbf{q}^{\text{MB}} = \rho \mathbf{u} [u^2 + T(D+2)], \quad (36)$$

$$\mathbf{R}^{\text{MB}} = \rho T [(D+2)T + u^2] \mathbf{I} + \rho [(D+4)T + u^2] \mathbf{u} \mathbf{u}. \quad (37)$$

Here, an overline denotes symmetrization. While all pertinent equilibrium moments in the comoving reference frame are accurate, the same conclusion does not necessarily hold when a different, noncomoving, arbitrary reference frame $\bar{\lambda} = \{\bar{\mathbf{u}}, \bar{T}\}$ is used for the evaluation. Indeed, the crucial difference between various lattices rests with the frame invariance of the equilibrium moments.

In the noncomoving reference frame $\bar{\lambda}$, the equilibrium populations $f^{\text{eq},\bar{\lambda}}$ are no longer given by the simple expression

ρW_i but must be computed. This can easily be accomplished by the reference frame transformation,

$$f^{\text{eq},\bar{\lambda}} = \mathcal{G}_{i,\lambda}^{\bar{\lambda}} f^{\text{eq},\lambda} = \rho \mathcal{G}_{i,\lambda}^{\bar{\lambda}} W, \quad (38)$$

operating on the vector of the lattice weights W , from the comoving frame λ to the $\bar{\lambda}$ frame. By construction, the equilibrium moments in the $\bar{\lambda}$ frame match the MB moments, if they are frame invariant. For example, the following relation holds for a third-order Grad projection sustained by the $D2Q16$ lattice,

$$\mathbf{Q}^{\text{eq},\bar{\lambda}} = \sum_{i=0}^{Q-1} v_i^{\bar{\lambda}} \mathbf{v}_i^{\bar{\lambda}} v_i^{\bar{\lambda}} f_i^{\text{eq},\bar{\lambda}} = \mathbf{Q}^{\text{eq},\lambda} = \mathbf{Q}^{\text{MB}}. \quad (39)$$

However, deviations occur for higher-order moments, not included in the set of frame invariant moments. Continuing with the same example, the fourth-order equilibrium moment in the $\bar{\lambda}$ frame becomes

$$\mathbf{R}^{\text{eq},\bar{\lambda}} = \mathbf{R}^{\text{MB}} + \mathbf{R}'. \quad (40)$$

The explicit form of the deviation can be computed via algebraic manipulations of Eqs. (37) and (38),

$$\mathbf{R}' = -\rho \{\xi \xi \xi^2 + \theta [(D+2)\theta \mathbf{I} + \xi^2 \mathbf{I} + (D+4)\xi \xi]\}, \quad (41)$$

where

$$\xi = \mathbf{u} - \bar{\mathbf{u}}, \quad \theta = T - \bar{T}. \quad (42)$$

As indicated by the previous expressions, the deviations vanish when the monitoring reference frame $\bar{\lambda}$ approach the comoving reference frame λ .

2. Full invariant moment system

Let us consider the case where the isotropy of the lattice supports the frame invariance of moments, up to fourth order. This case corresponds, in particular, to the $D2Q25$ lattice mentioned in Table I. The zeroth-order moment evaluation of Eq. (21) leads to the following equation,

$$\partial_t^{(1)} \rho^{\text{eq},\bar{\lambda}} + \nabla \cdot \mathbf{J}^{\text{eq},\bar{\lambda}} = 0, \quad (43)$$

where

$$\rho^{\text{eq},\bar{\lambda}} = \sum_{i=0}^{Q-1} \mathcal{G}_{i,\lambda}^{\bar{\lambda}} f^{\text{eq},\lambda}, \quad (44)$$

$$\mathbf{J}^{\text{eq},\bar{\lambda}} = \sum_{i=0}^{Q-1} v_i^{\bar{\lambda}} \mathcal{G}_{i,\lambda}^{\bar{\lambda}} f^{\text{eq},\lambda}. \quad (45)$$

Both moments belong to the frame invariant system of the reference frame transformation. As such, they can be evaluated equally well at the comoving reference frame,

$$\rho^{\text{eq},\bar{\lambda}} = \rho^{\text{eq},\lambda} = \rho, \quad (46)$$

$$\mathbf{J}^{\text{eq},\bar{\lambda}} = \mathbf{J}^{\text{eq},\lambda} = \rho \mathbf{u}. \quad (47)$$

We substitute Eqs. (46) and (47) into Eq. (43) and recover the continuity equation,

$$\partial_t^{(1)} \rho + \nabla \cdot (\rho \mathbf{u}) = 0. \quad (48)$$

The same reasoning applies to the rest of the conserved moments of Eq. (21), since all pertinent moments are frame

invariant. The momentum and energy conservation laws at the Euler level are as follows:

$$\partial_t^{(1)}(\rho\mathbf{u}) + \nabla \cdot \mathbf{P}^{\text{MB}} = 0, \quad (49)$$

$$\partial_t^{(1)}(2\rho E) + \nabla \cdot \mathbf{q}^{\text{MB}} = 0. \quad (50)$$

Analogously, the moments of the second-order equation (22) recover the Navier–Stokes–Fourier (NSF) contributions,

$$\partial_t^{(2)}\rho = 0, \quad (51)$$

$$\partial_t^{(2)}(\rho\mathbf{u}) + \nabla \cdot \mathbf{P}^{(1)} = 0, \quad (52)$$

$$\partial_t^{(2)}(2\rho E) + \nabla \cdot \mathbf{q}^{(1)} = 0, \quad (53)$$

where

$$\mathbf{P}^{(1)} = -\tau_1(\partial_t^{(1)}\mathbf{P}^{\text{MB}} + \nabla \cdot \mathbf{Q}^{\text{MB}}), \quad (54)$$

$$\mathbf{q}^{(1)} = -\tau_1(\partial_t^{(1)}\mathbf{q}^{\text{MB}} + \nabla \cdot \mathbf{R}^{\text{MB}}). \quad (55)$$

The compressible NSF equations are recovered from the summation of the $O(\epsilon^1)$, $O(\epsilon^2)$ contributions,

$$\partial_t\rho = -\nabla \cdot (\rho\mathbf{u}), \quad (56)$$

$$\partial_t(\rho\mathbf{u}) = -\nabla \cdot (\rho\mathbf{u}\mathbf{u}) - \nabla \cdot \boldsymbol{\pi}, \quad (57)$$

$$\partial_t(\rho E) = -\nabla \cdot (\rho E\mathbf{u}) - \nabla \cdot \mathbf{q} - \nabla \cdot (\boldsymbol{\pi} \cdot \mathbf{u}), \quad (58)$$

where $\boldsymbol{\pi}$ is the pressure tensor,

$$\boldsymbol{\pi} = \rho T \mathbf{I} - \mu \left(\mathbf{S} - \frac{2}{D} (\nabla \cdot \mathbf{u}) \mathbf{I} \right), \quad (59)$$

\mathbf{S} the strain rate tensor,

$$\mathbf{S} = \nabla\mathbf{u} + \nabla\mathbf{u}^\top, \quad (60)$$

\mathbf{q} is the heat flux,

$$\mathbf{q} = -\kappa \nabla T, \quad (61)$$

and viscosity and thermal conductivity are

$$\mu = \tau_1 \rho T, \quad (62)$$

$$\kappa = \tau_1 \rho C_p T, \quad (63)$$

where C_p is the specific heat at constant pressure.

3. Third-order invariant moment system

We continue with the analysis of a third-order moment invariant system, which corresponds to the $D2Q16$ lattice. The Euler level dynamics and the NSF density and momentum contributions include moments which are frame invariant. Thus, Eqs. (49) and (50) and the NSF density and momentum contributions (51) and (52) are obtained accurately. However, the NSF energy contribution includes the flux of energy flux tensor, which is not frame invariant. The evaluation of this moment at the monitoring frame $\bar{\lambda}$, instead of the comoving frame λ , induces an error, as seen from Eq. (41). This deviation gives rise to a diffusive error term at the NSF energy equation (53),

$$\begin{aligned} \partial_t^{(2)}(2\rho E) = \nabla \cdot \tau_1 \left(\partial_t^{(1)}\mathbf{q}^{\text{MB}} + \nabla \cdot \mathbf{R}^{\text{MB}} \right. \\ \left. + \frac{\partial \mathbf{R}'}{\partial \mathbf{u}} \cdot \nabla \mathbf{u} + \frac{\partial \mathbf{R}'}{\partial T} \cdot \nabla T \right). \end{aligned} \quad (64)$$

As expected from this analysis, the $D2Q16$ lattice demonstrates excellent performance in inviscid Euler gas dynamic systems, even at the presence of very strong discontinuities. In the presence of important viscous effects, the error term [last term in Eq. (64)] will affect the accuracy of the solution. The magnitude of the error scales with the spatial variation of the reference frame, or in other words the gradients of the velocity and temperature field. As shown in subsequent numerical simulations, benchmark viscous hydrodynamic flows can be accurately captured with $D2Q16$ lattice, suggesting that the magnitude of the error term is rather weak. However, as the velocity and temperature gradients grow, the error terms manifests in the solution. Section VC provides further discussion on this topic, with the aid of numerical simulations.

4. Second-order invariant moment system

Finally, we examine the hydrodynamic properties of a second-order frame invariant moment system, with a representative example being the $D2Q9$ lattice. Such a model cannot support the full energy flux tensor and higher-order tensors (\mathbf{Q} , \mathbf{R}) as frame invariant moments. Following the same reasoning with the previous cases, we observe that error terms are introduced in the energy equation of the Euler-level dynamics (50) and the momentum and energy equations of the NSF-level dynamics (52) and (53). For relatively smooth flows without shocks, numerical evidence suggests that the effect of the error terms of the $D2Q9$ model is rather small. A prominent example is the case of an advected vortex, which has been shown to be captured accurately even for vortex and advection Mach numbers in the range of $\text{Ma}_v = 0.8$ and $\text{Ma}_a = 100$ [48]. However, for hydrodynamic flows with shocks, the errors due to the frame variation are non-negligible. Importantly, the shock dynamics at the Euler level are not described accurately, which translate into errors in the shock propagation speed.

5. Summary of observations

We summarize the domain of validity of the kinetic model, according to the order of the frame invariant moment system:

(1) Second-order ($D2Q9$): appropriate for smooth regions of compressible flows.

(2) Third-order ($D2Q16$): appropriate for shocked compressible flows, with small dissipation effects (Euler flows).

(3) Fourth-order ($D2Q25$): generally valid for NSF flows.

At this point we note that our observations, regarding the applicability domain of the different lattices, are consistent with a detailed study of the semi-Lagrangian PonD by Reyhanian [63]. The hierarchy relating the frame invariant moment system and its applicability serves as a basis to simplify the framework. In particular, the low-order model can be applied to the smooth regions of the flow and the high-order model in the regions of steep hydrodynamic gradients. In the following section, we discuss the coupling of the different models, in the spirit of Ref. [53].

E. Multiscale frame transformation

The Grad projection approach for the reference frame transformation is advantageous in terms of stability and

efficiency. In the following, we demonstrate an additional benefit, which is the deployment of different lattices throughout the domain with minimal change in the framework. In essence, we combine the core idea of the multiscale concept [53] along with the Grad projection frame transformation.

Let us consider two velocity sets of different order,

$$\mathcal{V}_q = \{\mathbf{c}_i^q, i = 0, \dots, q - 1\},$$

$$\mathcal{V}_Q = \{\mathbf{c}_i^Q, i = 0, \dots, Q - 1\},$$

where $q < Q$. We distinguish two different operations coupled with the frame transformation from λ to λ' :

(1) **Lifting:** The lifting operation switches from the lower-order q model to the higher-order Q model, requiring thus a map

$$f_q^\lambda \rightarrow f_Q^\lambda. \quad (65)$$

(2) **Projection:** The projection operation switches from the higher-order Q model to the lower-order q model, requiring thus a map

$$f_Q^\lambda \rightarrow f_q^\lambda. \quad (66)$$

The construction of both operations amounts to identifying the proper expansion coefficients of the Grad expansion. We recall that the expansion coefficients are function of the moments and the reference frame λ' .

1. Lifting

For the lifting operation, we can identify the list of moments $\mathbf{m}_{q \rightarrow Q}$, required for the reference frame transformation, as a composition,

$$\mathbf{m}_{q \rightarrow Q} = \{\mathbf{m}_q, \mathbf{m}_{Q-q}\}, \quad (67)$$

where \mathbf{m}_q is operationally available from f_q^λ and \mathbf{m}_{Q-q} constitutes the remaining unknown higher-order moments. The lifting operation consists in specifying the respective contributions as

$$\mathbf{m}_q = \mathcal{M}_{q,\lambda} f_q^\lambda, \quad (68)$$

$$\mathbf{m}_{Q-q} = \mathbf{m}_{Q-q}^{\text{eq}}, \quad (69)$$

where $\mathcal{M}_{q,\lambda}$ is the $q \times q$ matrix of the populations to moments map. With the required moments identified, the construction of the lifted populations proceeds similarly as in Sec. II B. The expansion coefficients are computed from the moments $\mathbf{m}_{q \rightarrow Q}$ and the reference frame λ' ,

$$\alpha_n = \alpha_n(\mathbf{m}_{q \rightarrow Q}; \lambda'). \quad (70)$$

The lifted populations $f_Q^{\lambda'}$ can then be found from Grad's expansion

$$f_{Q,i}^{\lambda'} = W_i^Q \sum_{n=0}^K \frac{1}{n!} \alpha^{(n)}(\mathbf{m}_{q \rightarrow Q}; \lambda') : \mathbf{H}^{(n)}(\mathbf{c}_i^Q), \quad (71)$$

where W_i^Q , $\mathbf{H}^{(n)}(\mathbf{c}_i^Q)$, and K are the weights, the Hermite polynomials, and the order of expansion of the high-order model, respectively. We note that equilibration of the remaining unknown higher-order moments is not a unique approach to describe a lifting operation. For example, the nonequilibrium components of the missing moments could be extrapolated

from neighboring points, as suggested in Ref. [64]. This approach, however, increases the complexity of the coupling and is prone to instabilities, especially for the case of an adaptive velocity set. On the other hand, the equilibration suggested in this work retains locality and stability for the lifting operation.

2. Projection

In the projection step, the high-order population f_Q^λ contains the subset of the q linearly independent moments, which is required for the construction of the low-order population $f_q^{\lambda'}$. Hence, in contrast with the lifting procedure, there is no missing information and the low-order moment vector $\mathbf{m}_{Q \rightarrow q}$ is operationally available from f_Q^λ ,

$$\mathbf{m}_{Q \rightarrow q} = \mathcal{M}_{Q,\lambda} f_Q^\lambda. \quad (72)$$

Similarly to the lifting operation, the projected populations $f_q^{\lambda'}$ are given by the Grad expansion,

$$f_{q,i}^{\lambda'} = W_i^q \sum_{n=0}^k \frac{1}{n!} \alpha^{(n)}(\mathbf{m}_{Q \rightarrow q}; \lambda') : \mathbf{H}^{(n)}(\mathbf{c}_i^q), \quad (73)$$

where W_i^q , $\mathbf{H}^{(n)}(\mathbf{c}_i^q)$, and k are the weights, the Hermite polynomials, and the order of expansion of the low-order model, respectively.

III. VARIABLE ADIABATIC EXPONENT AND PRANDTL NUMBER

A. Kinetic model

The kinetic model can be extended towards a variable adiabatic exponent via the two-population approach [41]. The second set of populations (g populations) is designed to carry the internal energy associated with nontranslational degrees of freedom and thus enable an adjustable adiabatic exponent $\gamma = C_p/C_v$, where $C_p = C_v + 1$ is the specific heat of ideal gas at constant pressure and C_v is the specific heat at constant volume [65,66]. The governing kinetic equations can be written as follows:

$$\partial_t f_i + \mathbf{v}_i \cdot \nabla f_i = \Omega_{f,i} = \frac{1}{\tau_1} (f_i^{\text{eq}} - f_i), \quad (74)$$

$$\partial_t g_i + \mathbf{v}_i \cdot \nabla g_i = \Omega_{g,i} = \frac{1}{\tau_1} (g_i^{\text{eq}} - g_i). \quad (75)$$

Additionally, the collision operators can accommodate an intermediate relaxation to quasi-equilibrium states, thus enabling a variable Prandtl number [41,67],

$$\Omega_{f,i} = \frac{1}{\tau_1} (f_i^{\text{eq}} - f_i) + \left(\frac{1}{\tau_1} - \frac{1}{\tau_2} \right) (f_i^* - f_i^{\text{eq}}), \quad (76)$$

$$\Omega_{g,i} = \frac{1}{\tau_1} (g_i^{\text{eq}} - g_i) + \left(\frac{1}{\tau_1} - \frac{1}{\tau_2} \right) (g_i^* - g_i^{\text{eq}}), \quad (77)$$

where f_i^* , g_i^* are the quasi-equilibria of the f and g populations and the relaxation time τ_2 determines the Prandtl number. The local conservation laws for the density ρ ,

momentum $\rho \mathbf{u}$, and total energy ρE are

$$\rho = \sum_{i=0}^{Q-1} f_i = \sum_{i=0}^{Q-1} f_i^{\text{eq}}, \quad (78)$$

$$\rho \mathbf{u} = \sum_{i=0}^{Q-1} \mathbf{v}_i f_i = \sum_{i=0}^{Q-1} \mathbf{v}_i f_i^{\text{eq}}, \quad (79)$$

$$\rho E = \sum_{i=0}^{Q-1} \frac{v_i^2}{2} f_i + \sum_{i=0}^{Q-1} g_i = \sum_{i=0}^{Q-1} \frac{v_i^2}{2} f_i^{\text{eq}} + \sum_{i=0}^{Q-1} g_i^{\text{eq}}, \quad (80)$$

where the total energy of ideal gas is

$$\rho E = C_v \rho T + \frac{\rho u^2}{2}. \quad (81)$$

The equilibrium populations in the comoving reference frame are as follows:

$$f_i^{\text{eq}} = \rho W_i, \quad (82)$$

$$g_i^{\text{eq}} = \left(C_v - \frac{D}{2} \right) T \rho W_i. \quad (83)$$

The expressions for the dynamic viscosity, bulk viscosity, and thermal conductivity are [41]

$$\mu = \tau_1 \rho T, \quad (84)$$

$$\zeta = \left(\frac{1}{C_v} - \frac{2}{D} \right) \mu, \quad (85)$$

$$\kappa = \tau_2 \rho C_p T. \quad (86)$$

The Prandtl number is therefore

$$\text{Pr} = \frac{C_p \mu}{\kappa} = \frac{\tau_1}{\tau_2}. \quad (87)$$

For $\text{Pr} < 1$, the quasi-equilibria are designed to conserve the centered heat flux, resulting in the following expressions:

$$f_i^* = f_i^{\text{eq}} + W_i \mathbf{Q} \cdot (\mathbf{e}_i \mathbf{e}_i \mathbf{e}_i - 3T \mathbf{e}_i \mathbf{I}) / 6T^3, \quad (88)$$

$$g_i^* = g_i^{\text{eq}} + W_i \boldsymbol{\zeta} \cdot \mathbf{e}_i / T, \quad (89)$$

where $\mathbf{e}_i = \mathbf{v}_i - \mathbf{u}$, \mathbf{Q} is the nonequilibrium third-order flux tensor, and $\boldsymbol{\zeta}$ is the energy flux associated with the internal degrees of freedom,

$$\mathbf{Q} = \sum_{i=0}^{Q-1} \mathbf{e}_i \mathbf{e}_i \mathbf{e}_i (f_i - f_i^{\text{eq}}), \quad (90)$$

$$\boldsymbol{\zeta} = \sum_{i=0}^{Q-1} \mathbf{e}_i (g_i - g_i^{\text{eq}}). \quad (91)$$

B. Comments on g populations

We note that the concepts presented so far apply equally well for the g populations, with the sole difference being the required frame invariant moments, which have to be supported by the corresponding g lattice. A Chapman–Enskog analysis [41] shows that g equilibrium moments up to second order are enough to recover the NSF equations. Therefore, the $D2Q9$ is employed in this work for the g populations. The reference frame transformation (Sec. II B) and its multiscale realization (Sec. II E) apply equally well for the g populations,

taking into account that the maximal frame invariant moment is second order.

IV. NUMERICAL IMPLEMENTATION

A. Finite-volume discretization

We proceed with the finite-volume discretization, in the spirit of PonD-DUGKS framework [56,57]. In accord with the notions above, the kinetic equation can be formulated in an arbitrary reference frame λ . We first present the discretization for $\text{Pr} = 1$. The extension for variable Prandtl number is explained in the following section.

1. Updating rule

The evolution of the kinetic model (74) and (75) can be discretized as follows:

$$\begin{aligned} \tilde{f}_i^\lambda(\mathbf{x}_j, t_{n+1}) &= \left(\frac{2\tau - \delta t}{2\tau + \delta t} \right) \tilde{f}_i^\lambda(\mathbf{x}_j, t_n) \\ &+ \left(\frac{2\delta t}{2\tau + \delta t} \right) f_i^{\text{eq},\lambda}(\mathbf{x}_j, t_n) - \frac{\delta t}{V_j} F_{f,i}^\lambda(\mathbf{x}_j, t_{n+1/2}), \end{aligned} \quad (92)$$

$$\begin{aligned} \tilde{g}_i^\lambda(\mathbf{x}_j, t_{n+1}) &= \left(\frac{2\tau - \delta t}{2\tau + \delta t} \right) \tilde{g}_i^\lambda(\mathbf{x}_j, t_n) \\ &+ \left(\frac{2\delta t}{2\tau + \delta t} \right) g_i^{\text{eq},\lambda}(\mathbf{x}_j, t_n) - \frac{\delta t}{V_j} F_{g,i}^\lambda(\mathbf{x}_j, t_{n+1/2}). \end{aligned} \quad (93)$$

The update equations are derived from the integration of the continuous equations (74) and (75), formulated in the reference frame λ in a control volume centered at \mathbf{x}_j with volume V_j from time t_n to $t_{n+1} = t_n + \delta t$, using the midpoint rule for the convection term and the trapezoidal rule for the collision term [57]. To remove the implicitness, the DUGKS scheme adopts the variable transformation from the standard LBM practice [18,68],

$$\tilde{\phi}_i^\lambda = \phi_i^\lambda - \frac{\delta t}{2} \Omega_{\phi,i}^\lambda = \phi_i^\lambda - \frac{\delta t}{2\tau} (\phi_i^{\text{eq},\lambda} - \phi_i^\lambda), \quad (94)$$

where ϕ stands for the f and g populations and $\Omega_{\phi,i}$ are the collision BGK kernels defined in Eqs. (74) and (75). The fluxes of the populations $F_{\phi,i}^\lambda(\mathbf{x}_j, t_{n+1/2})$ across the surface of the control volume are defined as

$$F_{\phi,i}^\lambda(\mathbf{x}_j, t_{n+1/2}) = \int_{\partial V_j} (\mathbf{v}_i^\lambda \cdot \mathbf{n}) \phi_i^\lambda(\mathbf{x}, t_{n+1/2}) d\mathbf{S}, \quad (95)$$

where \mathbf{n} is the outward unit vector normal to the surface. Finally, we remark that, within the finite-volume context, the populations and the collision terms are cell-averaged quantities,

$$\phi_i^\lambda(\mathbf{x}_j, t_n) = \frac{1}{V_j} \int_{V_j} \phi_i^\lambda(\mathbf{x}, t_n) d\mathbf{x}. \quad (96)$$

The reference frame, which is used for the evolution of the populations at (\mathbf{x}_j, t_n) , is set to the comoving frame from the known flow velocity and temperature,

$$\lambda(\mathbf{x}_j, t_n) = \{\mathbf{u}(\mathbf{x}_j, t_n), T(\mathbf{x}_j, t_n)\}. \quad (97)$$

2. Flux evaluation

The key element of the update equations (92) and (93) is the evaluation of the flux term $F_{\phi,i}^{\lambda}(\mathbf{x}_j, t_{n+1/2})$, which contains the unknown populations $\phi_i^{\lambda}(\mathbf{x}_b, t_{n+1/2})$ at the cell interface \mathbf{x}_b and time $t_{n+1/2}$. The frame which shall be used for the flux evaluation is $\lambda_F = \{\mathbf{u}_F, T_F\}$, with the frame velocity \mathbf{u}_F and temperature T_F constructed by the average frame of the adjacent cell centers to the interface $\mathbf{x}_1, \mathbf{x}_2$,

$$\mathbf{u}_F = \frac{1}{2}[\mathbf{u}(\mathbf{x}_1, t_n) + \mathbf{u}(\mathbf{x}_2, t_n)], \quad (98)$$

$$T_F = \frac{1}{2}[T(\mathbf{x}_1, t_n) + T(\mathbf{x}_2, t_n)]. \quad (99)$$

The integration of Eqs. (74) and (75) along the characteristics for half-time step shows that the required populations $\phi_i^{\lambda_F}(\mathbf{x}_b, t_{n+1/2})$ are connected with the known populations at time t_n through the following equation [57]:

$$\bar{\phi}_i^{\lambda_F}(\mathbf{x}_b, t_{n+1/2}) = \bar{\phi}_i^{+\lambda_F}(\mathbf{x}_b - \mathbf{v}_i^{\lambda_F} \delta t/2, t_n), \quad (100)$$

where

$$\bar{\phi}_i^{\lambda_F} = \phi_i^{\lambda_F} - \frac{\delta t/2}{2} \Omega_{\phi,i}^{\lambda_F}, \quad (101)$$

$$\bar{\phi}_i^{+\lambda_F} = \phi_i^{\lambda_F} + \frac{\delta t/2}{2} \Omega_{\phi,i}^{\lambda_F}. \quad (102)$$

Equation (100) is essentially a half-time semi-Lagrangian step, with the final point located at the interface \mathbf{x}_b , at $t_{n+1/2}$. The populations $\bar{\phi}_i^{+\lambda_F}$ and the spatial gradients $\sigma_i^{\lambda_F} = \nabla \bar{\phi}_i^{+\lambda_F}$ are subsequently evaluated in the neighboring cells of the interface, at time t_n . In this work, Van Leer and minmod slope limiters were used for the computation of the spatial derivatives [69,70]. We also note that the reference frame transformation was applied to express the required populations from their original reference frame to the target reference frame λ_F . The populations are reconstructed at the departure point $\mathbf{x}' = \mathbf{x}_b - \mathbf{v}_i^{\lambda_F} \delta t/2$, with the MUSCL scheme [71],

$$\bar{\phi}_i^{+\lambda_F}(\mathbf{x}', t_n) = \bar{\phi}_i^{+\lambda_F}(\mathbf{x}_j, t_n) + (\mathbf{x}' - \mathbf{x}_j) \cdot \sigma_i^{\lambda_F}(\mathbf{x}_j, t_n). \quad (103)$$

According to Eq. (100), we obtain the $\bar{\phi}_i^{\lambda_F}$ populations at the interface \mathbf{x}_b and time $t_{n+1/2}$,

$$\bar{\phi}_i^{\lambda_F}(\mathbf{x}_b, t_{n+1/2}) = \bar{\phi}_i^{+\lambda_F}(\mathbf{x}', t_n). \quad (104)$$

The density, momentum, and temperature at $(\mathbf{x}_b, t_{n+1/2})$ are finally computed by

$$\rho = \sum_{Q,i=0}^{Q-1} \bar{f}_i^{\lambda_F}(\mathbf{x}_b, t_{n+1/2}), \quad (105)$$

$$\rho \mathbf{u} = \sum_{i=0}^{Q-1} \mathbf{v}_i^{\lambda_F} \bar{f}_i^{\lambda_F}(\mathbf{x}_b, t_{n+1/2}), \quad (106)$$

$$C_v \rho T = \sum_{i=0}^{Q-1} \frac{(v_i^{\lambda_F})^2}{2} \bar{f}_i^{\lambda_F}(\mathbf{x}_b, t_{n+1/2}) + \sum_{i=0}^{Q-1} \bar{g}_i^{\lambda_F}(\mathbf{x}_b, t_{n+1/2}) - \frac{\rho u^2}{2}. \quad (107)$$

With the calculated macroscopic fields (ρ, \mathbf{u}, T) at $(\mathbf{x}_b, t_{n+1/2})$, the equilibrium populations $\phi_i^{\text{eq},\lambda_F}(\rho, \mathbf{u}, T)$ can be computed and subsequently also the populations

$\phi_i^{\lambda_F}(\mathbf{x}_b, t_{n+1/2})$, after inversion of Eq. (101). We remind that the equilibrium populations can be obtained through the reference frame transformation (38),

$$\phi_i^{\text{eq},\lambda_F}(\rho, \mathbf{u}, T) = \rho \mathcal{G}_{\{\mathbf{u}, T\}}^{\{\mathbf{u}_F, T_F\}} W. \quad (108)$$

Finally, the fluxes which are required to update the cell centers populations can be found from summation over the faces of the cell and proper reference frame transformation,

$$F_{\phi,i}^{\lambda}(\mathbf{x}_j, t_{n+1/2}) = \sum_c (\mathbf{v}_i^{\lambda} \cdot \mathbf{n}_c) \mathcal{G}_{\{i, \lambda_F, c\}}^{\lambda} \phi_i^{\lambda_F, c}(\mathbf{x}_{b,c}, t_{n+1/2}), \quad (109)$$

where $\mathbf{x}_{b,c}$ designates the center of the c th face of the cell, \mathbf{n}_c is the outwards normal vector and λ is the reference frame of the evolution of the cell.

3. Summary of the algorithm

Based on the previous steps, we summarize the evolution procedure from time t_n to t_{n+1} :

(1) Initial data (cell centers \mathbf{x}_j)

(a) Given (ρ, \mathbf{u}, T) , comoving reference frame $\lambda = \{\mathbf{u}(\mathbf{x}_j, t_n), T(\mathbf{x}_j, t_n)\}$ and populations $\phi_i^{\lambda}(\mathbf{x}_j, t_n)$.

(b) Calculate the $\bar{\phi}_i^{+\lambda}(\mathbf{x}_j, t_n)$ populations according to Eq. (102).

(2) Calculation of the fluxes (loop over cell faces \mathbf{x}_b)

(a) Set reference frame λ_F at interface and time $(\mathbf{x}_b, t_{n+1/2})$.

(b) Calculate the populations $\bar{\phi}_i^{\lambda_F}(\mathbf{x}_b, t_{n+1/2})$ according to procedure in Sec. IV A 2.

(3) Population update (loop over cell centers \mathbf{x}_j)

(a) Compute the fluxes to the local reference frame of the cell, Eq. (109), and update the populations through Eqs. (92) and (93).

We stress the crucial difference between the proposed realization and the scheme suggested in Ref. [56], which is the absence of iterations within the flux evaluation step. We remind the reader that, according to Eq. (100), a semi-Lagrangian step is executed to retrieve the populations at the cell faces. In this work, the reference frame for the above step is set from the average reference frames of the neighboring cell centers [Eq. (98)] and the flux evaluation is performed explicitly. With this approach, it is necessary to obtain noncomoving equilibrium populations $\phi_i^{\text{eq},\lambda_F}(\rho, \mathbf{u}, T)$ to finalize the flux evaluation. The scheme in Ref. [56] suggested an iterative predictor-corrector procedure, such that the flux calculation is realized in the comoving reference frame. While computationally demanding, the iteration procedure operates only with the simple comoving equilibrium populations [Eqs. (82) and (83)]. A further analysis of this aspect via numerical simulations is provided in Sec. V E.

B. Implementation of variable Prandtl number

The quasi-equilibrium relaxation can be implemented as a forcing term in the kinetic equations. We follow a typical approach in the context of DUGKS [59] and realize the quasi-equilibrium relaxation via the Strang-splitting method [72]:

(1) Quasi-equilibrium relaxation of the populations in the cell centers (half-time step),

$$f_i' = f_i + \frac{\delta t}{2} \left(\frac{1}{\tau_1} - \frac{1}{\tau_2} \right) (f_i^* - f_i^{\text{eq}}). \quad (110)$$

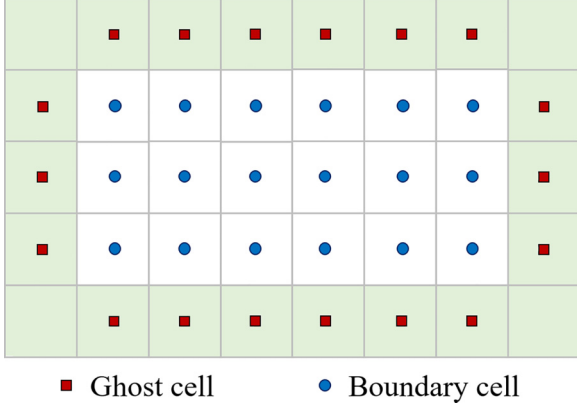


FIG. 1. Schematic for the implementation of boundary conditions.

(2) Update step without quasi-equilibrium relaxation, Eqs. (92) and (93).

(3) Quasi-equilibrium relaxation of the populations in the cell centers (half-time step), as in step 1.

We note that half-time relaxations steps occur in each cell center and are local operations. By construction, the quasi-equilibrium relaxation conserves the flow velocity and temperature, and the populations remain in their comoving reference frame.

C. Multiscale implementation

The presented framework can be implemented in a multiscale setting with minimal changes in the algorithm. The different lattices are deployed adaptively in the simulation domain following a switching criterion. According to Sec. IID, the switching criterion is a function of the hydrodynamic gradients, with the high-order lattice being activated in the regions of steep gradients. In this work, the switching function consists of threshold criteria on the numerically computed flow velocity and temperature gradients. The different lattices are updated normally as presented in the previous section, with the difference being that the reference frame transformations in the vicinity of the interface regions are replaced by the multiscale frame transformations (presented in Sec. IIE).

D. Boundary conditions

The boundary conditions (BCs) are enforced in the current work via the ghost node approach [73]. First, the density, flow velocity, and temperature are determined at the ghost cell C_G (see Fig. 1). For fixed values at the wall, e.g., no-slip velocity \mathbf{u}_w , the value \mathbf{u}_G at the ghost cell is

$$\mathbf{u}_G = 2\mathbf{u}_w - \mathbf{u}_B, \quad (111)$$

where \mathbf{u}_B is the corresponding value at the boundary cell. To impose zero normal gradient condition, e.g., for density computation, we enforce

$$\rho_G = \rho_B. \quad (112)$$

With the macroscopic values ($\rho_G, \mathbf{u}_G, T_G$) defined, the reference frame of the ghost cell λ_G is set to the comoving reference frame, $\lambda_G = \{\mathbf{u}_G, T_G\}$. The equilibrium populations

are then

$$f_i^{G,\text{eq}} = \rho_G W_i, \quad (113)$$

$$g_i^{G,\text{eq}} = \left(C_v - \frac{D}{2} \right) T_G \rho_G W_i. \quad (114)$$

The approximation of nonequilibrium contributions follows the implementation of Ref. [41]. In particular, the first-order nonequilibrium moments are estimated from the Chapman–Enskog solution, and they depend on the local hydrodynamic gradients. The pertinent nonequilibrium moments of the f populations are [41]

$$\mathbf{P}^{(1)} = -\tau_1 \rho_G T_G \left(\mathbf{S} - \frac{1}{C_v} (\nabla \cdot \mathbf{u}) \mathbf{I} \right), \quad (115)$$

$$\mathbf{Q}^{(1)} = -\tau_2 \rho_G T_G (\overline{\nabla T \mathbf{I}}) + \overline{\mathbf{u} \mathbf{P}^{(1)}}. \quad (116)$$

The zeroth-order up to second-order nonequilibrium moments of the g populations, $M_{g,0}^{(1)}, M_{g,1}^{(1)}, M_{g,2}^{(1)}$ are estimated as [41]

$$M_{g,0}^{(1)} = -\tau_1 \rho_G T_G (2C_v - D) \left(\frac{1}{C_v} \nabla \cdot \mathbf{u} \right), \quad (117)$$

$$M_{g,1}^{(1)} = -\tau_2 \rho_G T_G (2C_v - D) \nabla T + M_{g,0}^{(1)} \mathbf{u}, \quad (118)$$

$$M_{g,2}^{(1)} = -\tau_1 \rho_G T_G (2C_v - D) (T \mathbf{S} + \overline{\mathbf{u} \nabla T}). \quad (119)$$

The hydrodynamic gradients are evaluated with a second-order centered scheme based on previous time step quantities. The nonequilibrium populations are computed from their nonequilibrium moments according to Grad’s projection procedure,

$$f_i^{\lambda'} = W_i \sum_{n=0}^3 \frac{1}{n!} \boldsymbol{\alpha}^{(n)}(\mathbf{P}^{(1)}, \mathbf{Q}^{(1)}; \lambda_G) : \mathbf{H}^{(n)}(\mathbf{c}_i), \quad (120)$$

$$g_i^{\lambda'} = W_i \sum_{n=0}^2 \frac{1}{n!} \boldsymbol{\alpha}_g^{(n)}(M_{g,0}^{(1)}, M_{g,1}^{(1)}, M_{g,2}^{(1)}; \lambda_G) : \mathbf{H}^{(n)}(\mathbf{c}_i). \quad (121)$$

V. RESULTS AND DISCUSSION

In this section, we assess numerically the consistency of the adaptive reference frame formulation. The model is further validated with one- and two-dimensional (1D and 2D) Euler gas dynamics benchmarks and viscous flows to assess the Prandtl number as well as the accuracy of the wall BCs. Subsequently, we focus on the shock structure problem and demonstrate numerically the implications of the moment analysis of Sec. IID. The framework is then implemented with the multiscale setting (Sec. IIE), via the deployment of different lattices across the simulation domain. We conclude this section with a summary of our observations and discussion of the model capabilities. We remind the reader that the g populations evolve with the $D2Q9$ lattice. Unless stated otherwise, the numerical parameters of the simulations are the following: The time step δt is such that the Courant–Friedrichs–Lewy (CFL) number is $\text{CFL} = \max |v_{i\alpha}| (\delta t / \delta x) = 0.2$, where δx is the grid resolution. The adiabatic exponent is $\gamma = 1.4$. Additionally, the viscosity for the Euler flows is low enough such that the results remain invariant [typically $\mu \sim O(10^{-3} - 10^{-2})$]. Finally, we note that the formulation of the initial and boundary conditions are

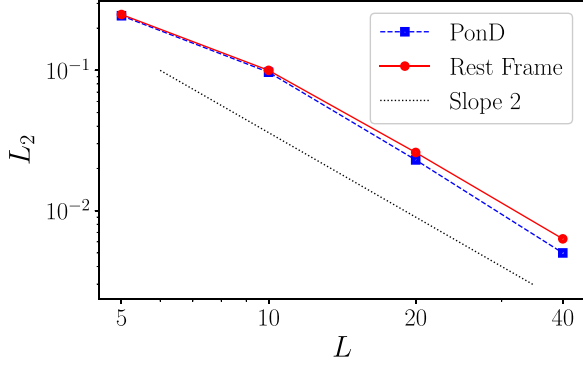


FIG. 2. Convergence order analysis (L_2 error norm) for the force driven flow over channel at $Re = 100$. Solid red line shows uniform frame “at rest.” Dashed blue line shows PonD. The dotted line indicates a second-order L_2 error norm slope.

based on nondimensional variables scaled with appropriate reference density, velocity, and pressure.

A. Adaptive reference frame consistency

A point which is raised in the context of adaptive particles velocities is that a straightforward implementation would lead to the wrong hydrodynamic equations [74]. The non-commutativity of the particles velocities with the temporal and spatial derivatives would result then to incorrect hydrodynamic equations. Even the continuity equation at the Euler level would contain nonphysical source terms. This analysis however does not apply in the context of our model, which achieves consistency through the action of the reference frame transformation. Given a sufficient number of frame invariant moments, the Euler or the full NSF hydrodynamic equations can be consistently recovered. To address this point numerically, we compare the performance of the PonD model with an implementation which imposes a global uniform frame “at rest” $\lambda_0 = \{\mathbf{0}, T_L\}$. The latter then reduces to the standard DUGKS algorithm

We begin with an isothermal channel flow with Reynolds number of $Re = 100$. The flow is driven by a constant force and the boundary conditions include no slip at the walls and periodic conditions in the flow direction. The L_2 error of both simulations, using PonD and the uniform frame at rest, was measured at steady state,

$$L_2 = \sqrt{\frac{\sum_x [u_x^n(x) - u_x^a(x)]^2}{\sum_x [u_x^a(x)]^2}}, \quad (122)$$

where the sum runs over the entire spatial domain and u_x^n, u_x^a are the x velocity from the simulation and analytical solution, respectively. Both simulations achieve second-order spatial convergence with very similar error magnitudes, as shown in Fig. 2.

We continue with the simulations of the Lax shock tube problem [75], under low spatial resolutions and high CFL number. The initial conditions are the following:

$$(\rho, u_x, p) = \begin{cases} (0.445, 0.698, 3.528), & 0 \leq x < 0.5 \\ (0.5, 0, 0.571), & 0.5 \leq x \leq 1. \end{cases} \quad (123)$$

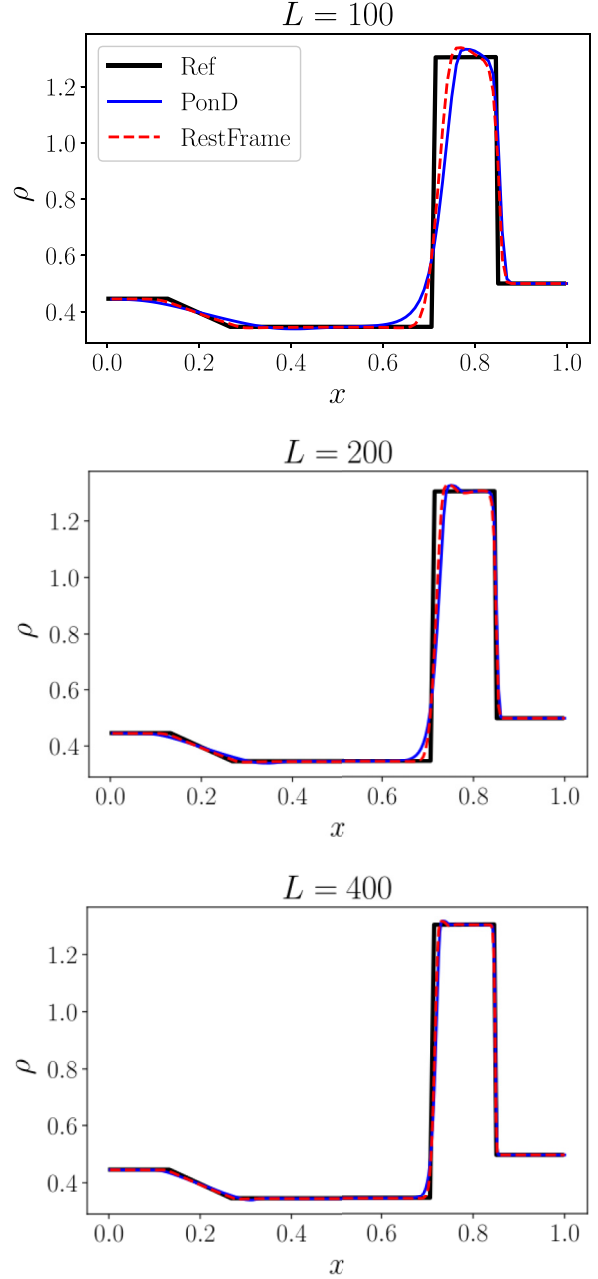


FIG. 3. Density profiles with different resolutions for the Lax shock tube problem at $t = 0.14$. Blue solid line shows PonD model. Red dashed line shows solution with a uniform reference frame “at rest” Black solid line shows reference from an exact Riemann solver.

The results with spatial resolutions, $L = 100, 200, 400$ and CFL number equal to 0.9 are shown in Fig. 3. We observe that, even at the lowest resolution, the solutions agree very well with each other. In particular, the solution from the PonD model is more dissipative, which can be attributed to the regularization stemming from the reference frame transformation. Apart from this, the shock propagation is almost indistinguishable. We note that such performance would be impossible, if the recovered hydrodynamic equations of our model did not match the Euler equations.

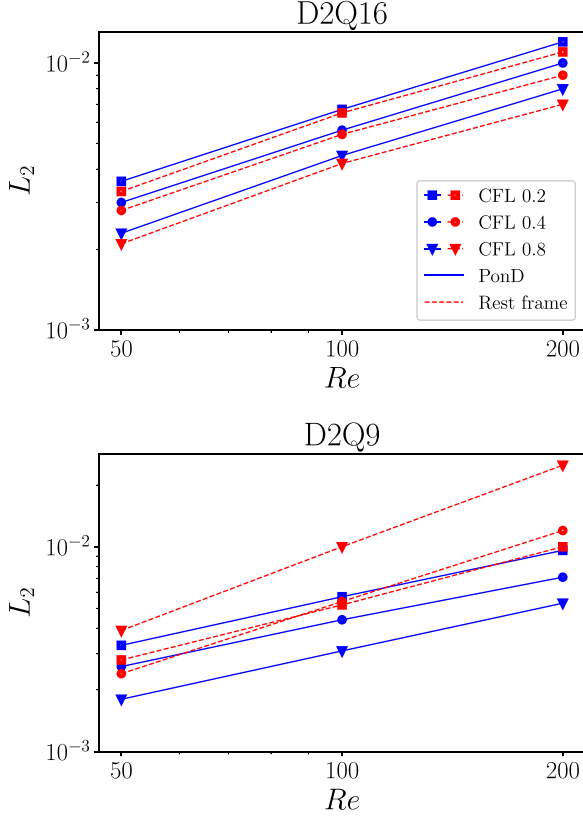


FIG. 4. Taylor–Green vortex problem: L_2 error norm for fixed spatial resolution [100×100] and varying CFL and Re number. The simulations were performed with the $D2Q16$ (top) and $D2Q9$ (bottom) velocity sets. Dashed red line shows uniform frame “at rest.” Solid blue line shows PonD.

To probe the temporal error under fixed spatial resolution we simulate the Taylor–Green vortex, which obeys the following analytical solution:

$$u_x(x, y, t) = -u_0 \cos(kx) \sin(ky) e^{-2\nu k^2 t}, \quad (124)$$

$$u_y(x, y, t) = u_0 \sin(kx) \cos(ky) e^{-2\nu k^2 t}, \quad (125)$$

$$p(x, y, t) = p_0 - \frac{\rho u_0^2}{4} [\cos(2kx) + \cos(2ky)] e^{-4\nu k^2 t}. \quad (126)$$

Here $k = 2\pi/L$ is the wave number while u_0 and p_0 are the initial values of velocity and pressure, respectively. The simulations were performed with a [100×100] grid using periodic boundary conditions. The initial maximum Mach number was fixed to $\text{Ma} = u_0/\sqrt{T_L} = 0.05$ and the L_2 error norm [see Eq. (122)] was recorded at half-life time, for different Re and CFL numbers. The results using the $D2Q16$ and $D2Q9$ velocity sets are summarized in Fig. 4. For the case of $D2Q16$, the error obtained with PonD and with the uniform frame at rest demonstrate the same dependence. The results are consistent with an extensive theoretical and numerical analysis of the errors of the DUGKS algorithm presented in Ref. [76]. The simulations of the PonD scheme with the $D2Q9$ lattice resulted in very similar errors. The corresponding results with the uniform rest-frame solution marked higher errors, with increasing Reynolds number.

We conclude this discussion with an estimate of the reduction in computational efficiency resulting from the adaptive reference frame formulation when compared with the uniform “rest-frame” case. For this purpose, we used the setup of the Lax shock tube on an eight-core PC without parallelization (Intel Core i7-9700@3GHz). We highlight that this test serves solely as an estimate and not as a comprehensive investigation of the computational efficiency. The velocity sets were the $D2Q16$ and the $D2Q9$, for the f and g populations, respectively. The results of the PonD model indicated a performance of 0.06 mega lattice updates per second (MLUPS), while the implementation with the uniform frame at rest achieved 0.4 MLUPS. Consequently, the reference frame transformation reduces the computational efficiency by a factor of 6.6.

B. Euler gas dynamics

We validate the model using the $D2Q16$ lattice and a third-order Grad projection for the moment transformation. According to the moment analysis in Sec. IID, the hydrodynamics at the Euler level should be captured accurately. Indeed, the model performs very well against a series of 1D Riemann problems, involving low-density near-vacuum regions and very strong discontinuities. While all benchmarks of the previous work [56] were tested, we present here two representative 1D examples. The 2D cases include a high Mach Riemann problem, a Mach 3 flow over a step obstacle, and a shock diffraction over a corner.

1. Strong shock tube

We consider the case of a strong shock tube [77], where the ratio between the temperature of the left and right side is 10^5 . The initial conditions for this problem are

$$(\rho, u_x, p) = \begin{cases} (1, 0, 1000), & 0 \leq x < 0.5 \\ (1, 0, 0.01), & 0.5 \leq x \leq 1. \end{cases} \quad (127)$$

This problem, characterized by the strong temperature discontinuity, probes the robustness and accuracy of the numerical methods. The results of the simulation at $t = 0.012$ and $L = 800$ are shown in Fig. 5. Overall, a very good agreement with the exact solution is noted. Simulations with low resolutions are summarized in Fig. 6.

2. Le Blanc problem

The Le Blanc problem is considered next [78] and involves very strong discontinuities and is initialized with the following conditions,

$$(\rho, u_x, p) = \begin{cases} (1, 0, 2/3 \times 10^{-1}), & 0 \leq x < 3 \\ (10^{-3}, 0, 2/3 \times 10^{-10}), & 3 \leq x \leq 9. \end{cases} \quad (128)$$

In this problem, the adiabatic exponent is fixed to $\gamma = 5/3$. Figure 7 shows the results at $t = 6$ and $L = 1000$. With the exception of minor oscillations, a very good agreement of the present scheme with the reference solution [14] is observed.

3. Two-dimensional Riemann, configuration 3

As a first validation in two dimensions we simulate a 2D Riemann problem, which is a classical benchmark for

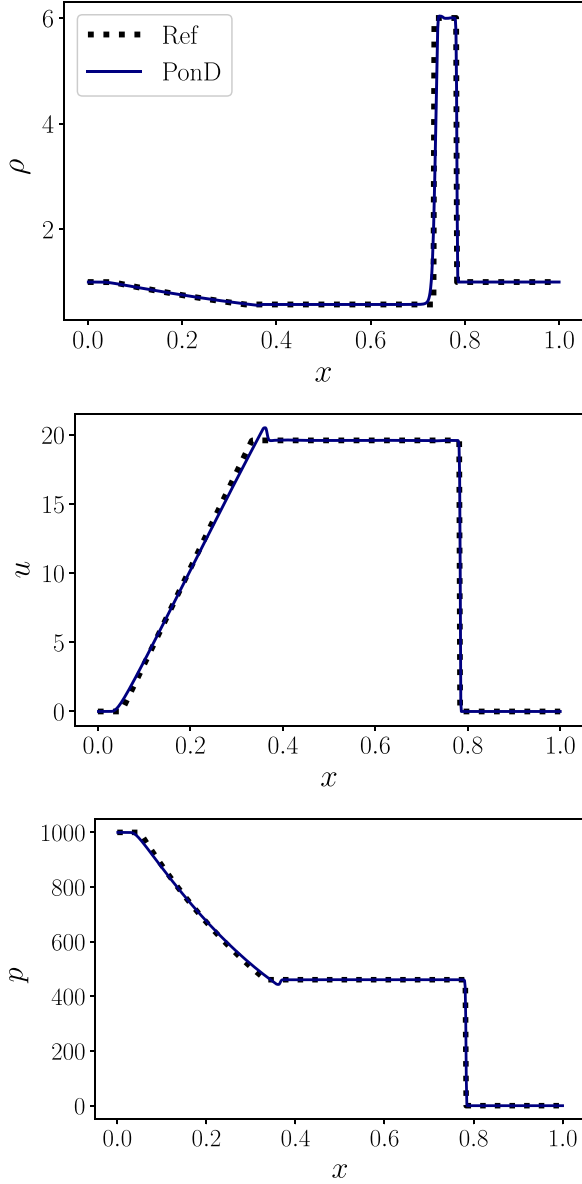


FIG. 5. Density (top), velocity (middle), and pressure (bottom) profiles for the strong shock tube problem at $t = 0.012$. Solid line shows PonD model. Dashed line shows reference from an exact Riemann solver.

compressible flow solvers [79]. A square domain $(x, y) \in [0, 1] \times [0, 1]$ is divided into four quadrants, each of which is initialized with constant values of density, velocity and pressure as follows:

$$(\rho, u_x, u_y, p) = \begin{cases} (1.5, 0, 0, 1.5), & x > 0.5, y > 0.5 \\ (0.5323, 1.206, 0, 0.3), & x \leq 0.5, y > 0.5 \\ (0.138, 1.206, 1.206, 0.029), & x \leq 0.5, y \leq 0.5 \\ (0.5323, 0, 1.206, 0.3), & x > 0.5, y \leq 0.5. \end{cases} \quad (129)$$

At the boundaries, zero-gradient BCs were imposed, $\partial_n f = 0$, where \mathbf{n} is the outwards unit normal vector. The simulation

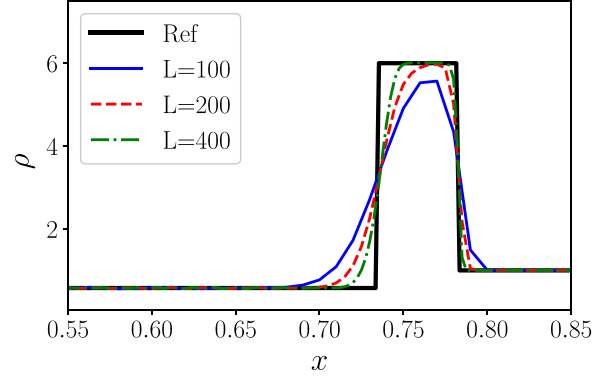


FIG. 6. Density profiles with different resolutions for the strong shock tube problem at $t = 0.012$. Solid blue line shows $L = 100$. Dashed red line shows $L = 200$. Dotted-dashed green line shows $L = 400$. Solid line shows reference from an exact Riemann solver.

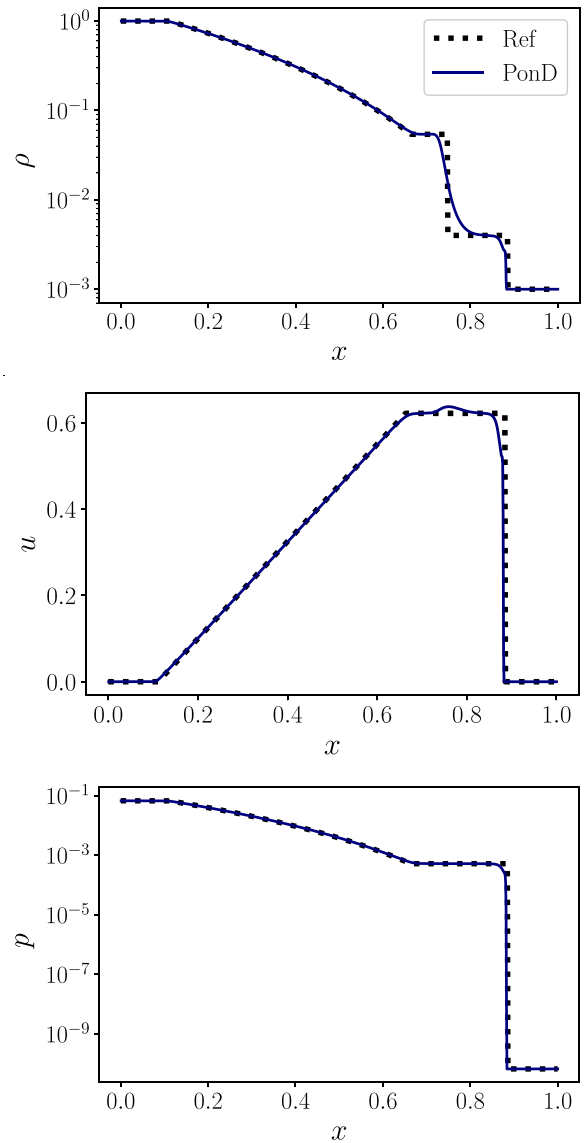


FIG. 7. Density (top), velocity (middle), and pressure (bottom) profiles for the Le Blanc problem, at $t = 6$. Solid line shows PonD model. Dashed line shows reference from an exact Riemann solver.

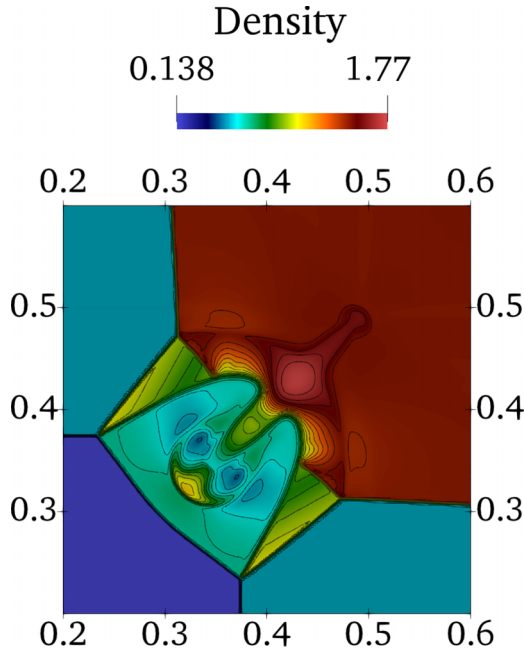


FIG. 8. 2D Riemann problem with resolution of [500,500] grid points at $t = 0.3$. Twenty-five equidistant density contours are superimposed on the results.

was performed with resolution [500,500]. The results of the density field, as well as density contours near the center of the domain, are depicted in Fig. 8. The initial conditions of the Riemann problem lead to shock wave interaction and the formation of complex patterns. The results show a very good agreement with the reference solutions in Refs. [79,80].

4. Mach 3 flow over step

In this problem, a uniform Mach 3 flow is imposed on a wind tunnel containing a step [81]. A transient shock wave develops from the step, reflects at the walls and forms a complicated flow pattern. The computational domain is bounded by a $[0, 3] \times [0, 1]$ rectangle, while the step is located at $(0.6, 0)$ and has a height of $\Delta y = 0.2$. Initially, a gas with $\gamma = 1.4$ is spatially uniform, with the following hydrodynamic conditions:

$$(\rho, u_x, u_y, p) = (1.4, 3, 0, 1). \tag{130}$$

The same conditions are imposed as inflow BCs at the left boundary $x = 0$ and outflow BCs at the right boundary $x = 3$. Reflecting BCs are applied at the walls of the domain. The results of a simulation resolved with [300,100] grid points are presented in Fig. 9, at six equal time intervals ($t = 0.5$ to $t = 3$). The flow features and dynamics are in very good agreement with the corresponding results from the literature [81].

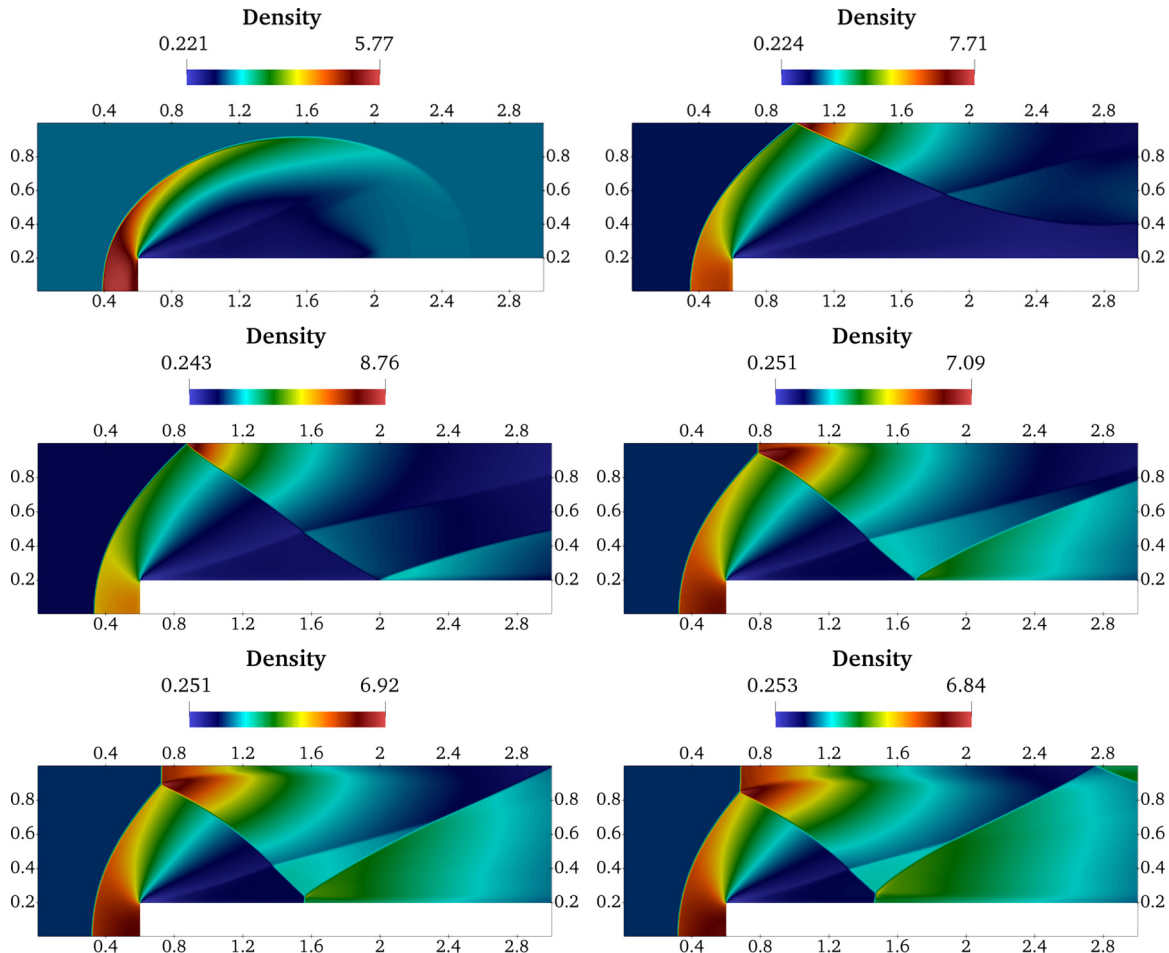


FIG. 9. Density profiles for the Mach 3 flow over forward step. Six snapshots are shown at equal time intervals from $t = 0$ to $t = 3$.

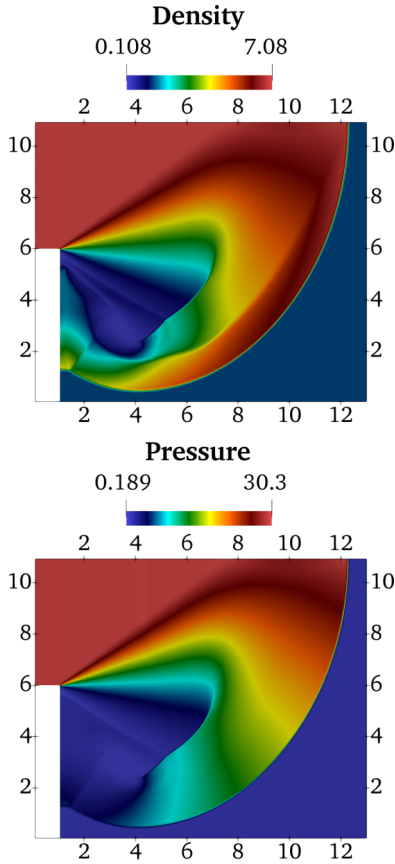


FIG. 10. Pressure (top) and density (bottom) profiles for the Mach 5.09 shock diffraction problem over a corner, at $t = 2.3$. 30 equidistant contours are superimposed on the fields.

5. Shock diffraction over corner

Here we investigate the shock diffraction problem, in which a shock wave flows over a backward facing corner [15]. The hydrodynamic patterns of this problem have been studied theoretically, experimentally, and via simulations. From the numerical standpoint however, this problem has been challenging due to the development of negative pressure and/or density around the corner. We follow the conventional setup of the problem: the computational domain consists of the union of $[0, 1] \times [6, 11]$ and $[1, 13] \times [0, 11]$ rectangles. Initially, a $Ma = 5.09$ right-moving shock wave is located at $x = 0.5$ and $6 \leq y \leq 11$ and propagates into undisturbed air, with density 1.4 and pressure 1. For the BCs, we use inflow with the initial conditions at $x = 0, 0 \leq y \leq 11$, outflow at $x = 13, 0 \leq y \leq 11$; $1 \leq x \leq 13, y = 0$; and $0 \leq x \leq 13, y = 11$. Reflective BCs are applied at the walls of the domain $0 \leq x \leq 1, y = 6$ and $x = 1, 0 \leq y \leq 6$. The results, for resolution [390, 330] and $t = 2.3$ are shown in Fig. 10 and compare very well with the reference results from Ref. [15].

C. Viscous flows

In this section, we focus on hydrodynamic flows with important viscous effects. The discussion pivots around the accuracy and the limitations of the third-order moment invariant system, sustained by the $D2Q16$ lattice.

1. Thermal Couette flow

The thermal Couette flow is a benchmark test case to probe the viscous heat dissipation and the Prandtl number. The upper wall with the higher temperature T_H is in motion with a constant speed u_0 , while the lower wall is at rest and at a temperature T_C . The analytical solution for the temperature is

$$\frac{T - T_C}{T_H - T_C} = \frac{x}{L} + \frac{\text{Pr} \times \text{Ec}}{2} \frac{x}{L} \left(1 - \frac{x}{L}\right), \quad (131)$$

where $\text{Ec} = u_0^2 / (C_p \Delta T)$ is the Eckert number and $\Delta T = T_H - T_C$. No-slip and constant-temperature BCs are applied at the top and bottom walls, while periodic BCs are enforced in the horizontal direction. The parameters for the simulations are $Ma = u_0 / \sqrt{\gamma T_C} = 0.5$, $L = 50$, $\text{Re} = \rho u_0 L / \mu = 100$, $T_C = 1$. Figure 11 shows the temperature profiles for three different Prandtl numbers ($\text{Pr} = 0.5, 0.75, 1.0$) and different Eckert numbers ($\text{Ec} = 4, 20, 40$), which are in very good agreement with the analytical solution. We note that the simulations have been performed with the $D2Q16$ lattice and thus a third-order Grad projection frame transformation. The accuracy of the results suggest that the error term in the energy equation (64) is negligibly small.

2. Viscous shock tube

In this problem we probe the performance of our model with the viscous shock tube test, proposed by Daru and Tenaud [82]. A 2D shock tube $[0, 1] \times [0, 1]$ is initialized with the following conditions:

$$(\rho, u_x, u_y, p) = \begin{cases} (120, 0, 0, 120/\gamma), & 0 \leq x < 0.5 \\ (1.2, 0, 0, 1.2/\gamma), & 0.5 \leq x \leq 1, \end{cases} \quad (132)$$

where $\gamma = 1.4$, the Prandtl number is set to $\text{Pr} = 0.73$, and the viscosity is set such that Reynolds number is $\text{Re} = 200$. No-slip and adiabatic BCs are applied at the walls of the shock tube. Due to the symmetric configuration of the problem, the actual simulated geometry consists of the $[0, 1] \times [0, 0.5]$ domain, with symmetric conditions applied on the top boundary. The initial flow conditions create a right propagating shock wave of $Ma = 2.37$, a contact discontinuity, and an expanding rarefaction wave in both directions. Note that the motion of the shock wave induces a non-negligible boundary layer along the horizontal wall of the tube. The boundary layer interacts with the incident and reflected shock, forming a complicated flow pattern.

The results of the density contours, the pressure and temperature fields for resolution of [500, 250] at $t = 1$, are shown in Fig. 12. Additionally, we repeat the simulation with the $D2Q25$ and a fourth-order frame invariant moment system and compare the results. For the comparison, we report metrics suggested from Ref. [83]. In particular, Table II summarizes the coordinates associated with the triple point and the primary vortex. The comparison with the reference data shows a very good match of both the $D2Q16$ and $D2Q25$ simulations. The same conclusion is drawn from Fig. 13, which plots the density distribution along the solid wall.

Finally, we include for completeness the results from the $\text{Re} = 1000$ case, simulated with a resolution of [2000, 1000] and the $D2Q16$ lattice (the $D2Q25$ solution is practically

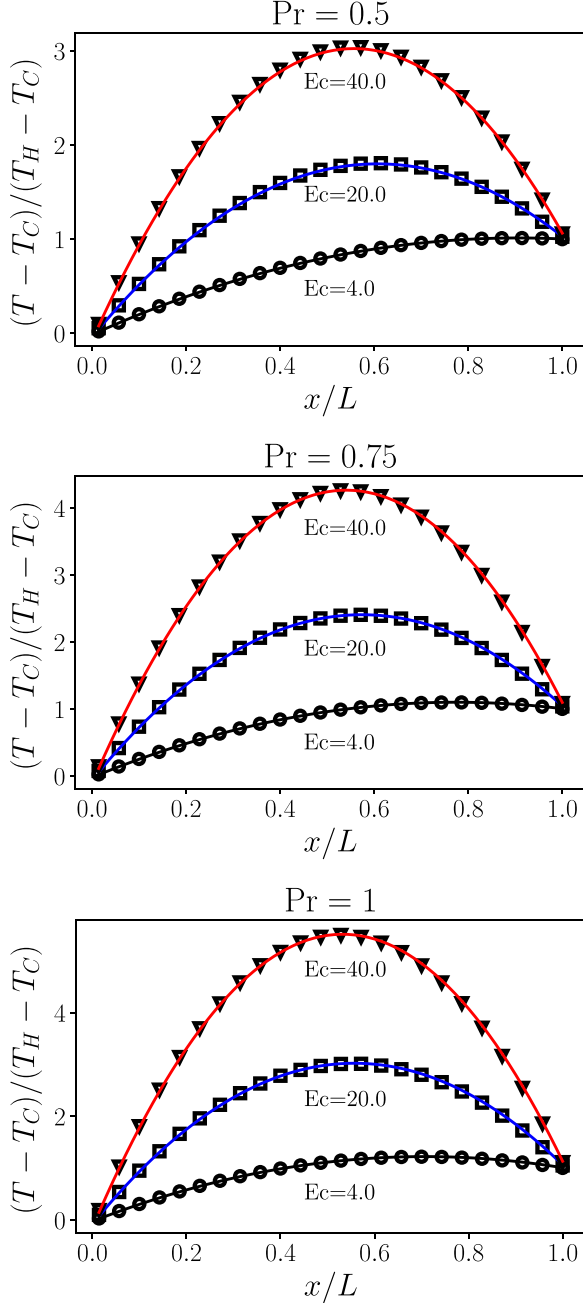


FIG. 11. Thermal Couette flow problem. Results are shown for three different Prandtl numbers: $Pr = 0.5$ (top), $Pr = 0.75$ (middle), $Pr = 1$ (bottom). For each Pr number, the simulation is performed for Eckert numbers $Ec = 4, 20, 40$ (symbols) and compared with analytical solution (solid lines).

indistinguishable). Figure 14 shows contours of the density field at $t = 1$ and the density distribution along the solid wall is compared with the reference solution from a high-order gas-kinetic solver in Fig. 15. While the main features of the flow are in line with corresponding reference solutions, noticeable deviations are present. Given that the PonD/DUGKS finite-volume scheme is second-order accurate, the grid-converged solution is hard to obtain due to practical limit on computational time of the present implementation. It is worth noting that even the results for high-order methods,

TABLE II. Accuracy criteria for viscous shock tube ($Re = 200$), according to Ref. [83]. x -TP (y -TP) correspond to the x coordinate (y coordinate) of the triple point. x -PV corresponds to the horizontal axis intersection of the line passing through the primary vortex. y -PV corresponds to the height of the primary vortex.

	x -TP	y -TP	x -PV	y -PV
Reference	0.58	0.137	0.78	0.166
D2Q16	0.58	0.133	0.774	0.168
D2Q25	0.58	0.134	0.775	0.168

from different papers or from different methods in the same paper, are very different [83].

3. Shock structure problem

The problems so far have demonstrated very good accuracy of the third-order frame invariant moment system and the associated $D2Q16$ lattice. The following benchmark involves steep hydrodynamic gradients and clearly demonstrates the limitations of the $D2Q16$. At the same time, the expansion of the frame invariant moment system from third-order to fourth-order ($D2Q25$) restores the accuracy.

The shock structure problem is a classical problem in kinetic theory of gases in which nonequilibrium effects dominate the flow [84]. We consider a quasi one-dimensional plane shock wave, with an initial step of density, velocity, and temperature at the center of the computational domain. The upstream and downstream flow values are connected through the Rankine–Hugoniot conditions [85]. The upstream mean-free path for hard-sphere molecules is defined as

$$\lambda_1 = \frac{16}{5\sqrt{2\pi\gamma}} \left(\frac{\mu_1 \alpha_1}{p_1} \right), \quad (133)$$

where p_1 , α_1 , μ_1 are the pressure, the speed of sound, and the viscosity of the gas upstream of the shock, respectively. The viscosity varies with the temperature as

$$\mu = \mu_1 \left(\frac{T}{T_1} \right)^s, \quad (134)$$

where, for the case of hard spheres, $s = 0.5$. The steady-state nondimensional density, temperature, normal stress, and heat flux are defined as follows:

$$\begin{aligned} \rho_n &= \frac{\rho - \rho_1}{\rho_2 - \rho_1}, & T_n &= \frac{T - T_1}{T_2 - T_1}, \\ \hat{\sigma}_{xx} &= \frac{\sigma_{xx}}{p_1}, & \hat{q}_x &= \frac{q_x}{p_1 \sqrt{2T_1}}, \end{aligned} \quad (135)$$

where the subscripts 1 and 2 indicate the upstream and downstream values, respectively. The Prandtl number is set to $Pr = 2/3$ and the adiabatic exponent of monatomic ideal gas to $\gamma = 5/3$. The results reported for this case are the steady-state solutions and compared with the results of Ohwada [86]. The origin of the coordinate system is the point with $\rho_n = 0.5$ and $x_n = x/0.5\sqrt{\pi}\lambda_1$ is used as the reduced coordinate.

We consider first the shock structure profiles for a Mach number $Ma = 1.2$. Two simulations are performed with different reference frame transformation orders. In particular, we compare the performance of the $D2Q16$ and $D2Q25$

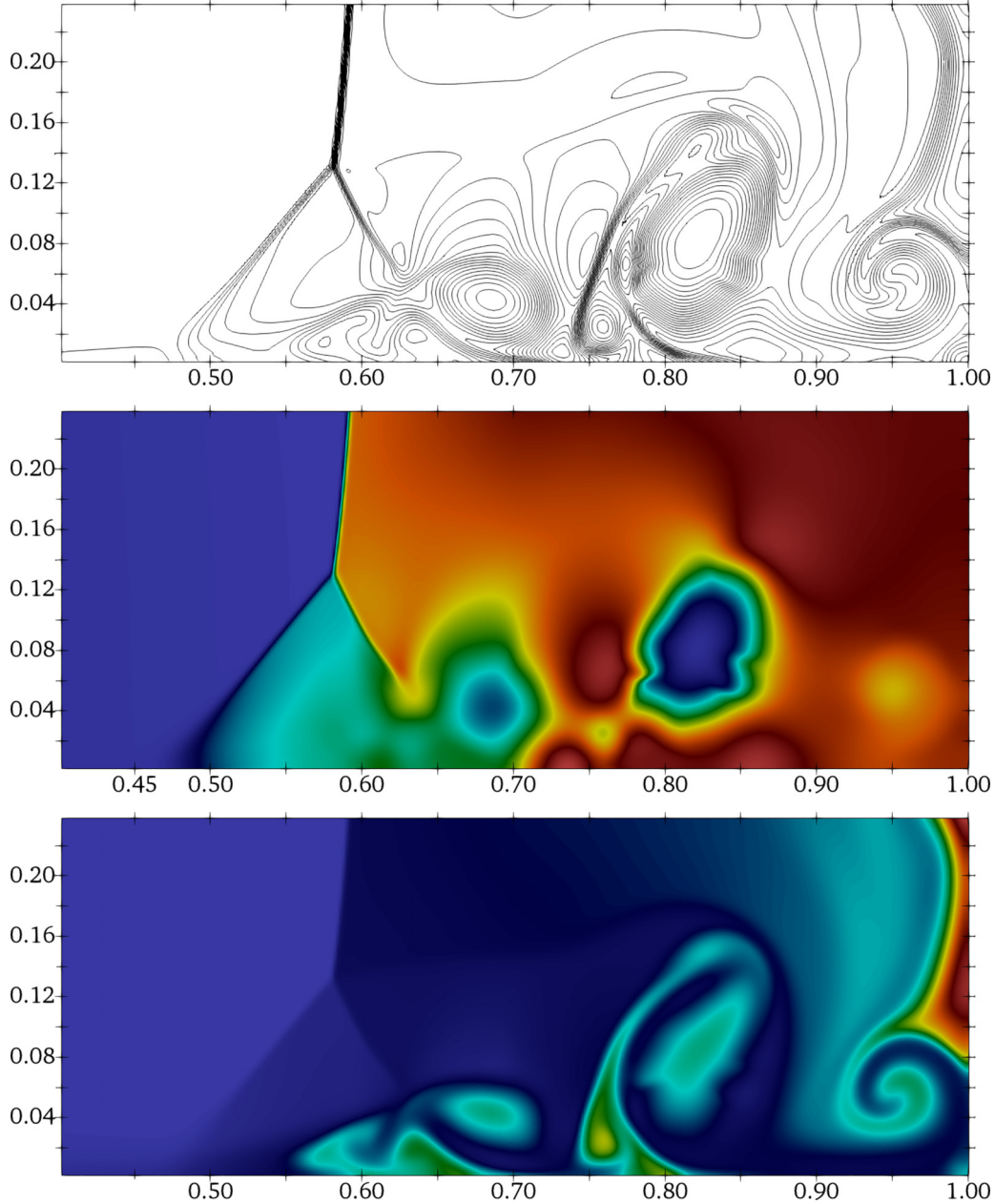


FIG. 12. Viscous shock tube problem ($Re = 200$). Top panel shows 30 equidistant density contours $\rho \in (18, 120)$. Middle panel shows pressure field $p \in (18, 89)$. Bottom panel shows temperature field $T \in (0.46, 2.84)$.

lattices, using third- and fourth-order Grad projections, respectively. The results for the density, temperature, normal stress, and heat flux profiles are shown in Fig. 16. It is evident that both models perform very accurately compared with the reference data.

We continue with the shock structure at a higher Mach of $Ma = 1.6$ and repeat the numerical experiments with the different frame transformation orders. The results are summarized in Fig. 17. Here, the third-order model clearly shows deviations in all the profiles, with the errors being prominent in the temperature and heat flux profiles, at the upstream part of the shock. In this case, the deviation terms due to the frame variant R^{eq} moment are sustained, due to the steep gradients of velocity and temperature within the shock profile. Including the R^{eq} moment list into the frame invariant list, i.e., the

fourth-order model, recovers the accuracy of the model and achieves very good agreement with the reference results.

D. Multiscale framework

The final topic of interest is the multiscale extension of the scheme, with the deployment of different lattices across the domain. The motivation is twofold: first, the target is to deploy the $D2Q9$ and $D2Q16$ lattices in Euler problems with steep discontinuities to numerically support the theoretical discussion of Sec. IID. In this case, the switching criterion is a threshold on the local flow velocity and temperature gradients. The high-order lattice is activated at the portion of the domain with high gradients, while the low-order lattice everywhere else. Subsequently, we apply the

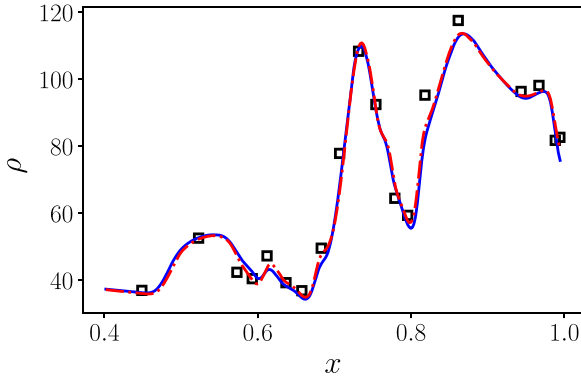


FIG. 13. Viscous shock tube problem ($Re = 200$). Density distribution along the solid wall. Solid line shows $D2Q16$ model. Dotted line shows $D2Q25$. Symbols show reference data from Ref. [83].

multiscale framework in problems with localized rarefaction phenomena. It is well known that higher-order lattices or equivalently higher-order Grad expansions of the distribution function can probe deeper into the nonequilibrium regime ($0.1 \lesssim Kn \lesssim 1$) [26,64,87,88]. A rigorous theoretical relation however between the Knudsen number and the number of moments is lacking. Unfortunately, however, it is known that Grad expansions converge rather slowly, with increasing number of moments [88]. While an expansion in Hermite polynomials is feasible in the transitional regime ($Kn \leq 1$), probing deeper into the nonequilibrium regime requires a change in strategy.

1. Lax tube

We demonstrate a $D2Q9$ - $D2Q16$ model, with the simulation of the Lax problem [75]. The initial conditions are the following:

$$(\rho, u_x, p) = \begin{cases} (0.445, 0.698, 3.528), & 0 \leq x < 0.5 \\ (0.5, 0, 0.571), & 0.5 \leq x \leq 1. \end{cases} \quad (136)$$

The simulation is performed with $L = 600$, until $t = 0.14$. Figure 18 shows the solution obtained by the $D2Q9$ and $D2Q16$ lattices independently. While the $D2Q16$ model is in excellent agreement with the analytical solution, the $D2Q9$ model develops deviations, which manifest as overestimated density between the shock wave and the contact discontinuity. The discrepancy in the Euler level is expected for the case of $D2Q9$ and therefore a second-order moment invariant system. Figure 19 shows the results of the multiscale $D2Q9$ - $D2Q16$ model and the regions of deployment of the two lattices. In particular, $D2Q16$ is active in two thin regions, centered at the shock wave and the contact discontinuity. The results of the multiscale model match again very well with the analytical solution.

2. Shu-Osher problem

The $D2Q9$ - $D2Q16$ model is further tested with the Shu-Osher problem [89]. In this setup, a Mach 3 shock wave interacts with a perturbed density field. The interaction leads to discontinuities and the formation of small structures. The

initial conditions are

$$(\rho, u_x, p) = \begin{cases} (3.857, 2.629, 10.333), & 0 \leq x < 1 \\ (1 + 0.2 \sin[5(x - 5)], 0, 1), & 1 \leq x \leq 10. \end{cases} \quad (137)$$

The results for the density profile are presented at $t = 1.8$ and $L = 800$. Figure 20 shows the solutions of the $D2Q9$ and $D2Q16$ models and the comparison with a reference solution, obtained with characteristic-based fifth-order WENO, RK4 temporal integration and resolution of 5000 points [90]. Apart from a small underestimation of the postshock waves amplitudes, it is evident that the $D2Q16$ captures very well the shock location and the high-frequency waves. In contrast, the $D2Q9$ model clearly deviates from the reference solution. Figure 21 captures the evolution of the $D2Q9$ - $D2Q16$ solution and compares it with the pure $D2Q16$ solution. The multiscale model is almost indistinguishable from the $D2Q16$ model and thus with the reference solution also. It is also interesting to observe that $D2Q16$ is activated only in narrow regions of the domain, as shown by the spikes in Fig. 21.

3. High Mach astrophysical jet

Here we consider an astrophysical jet of Mach 30, without radiative cooling [13]. This case is an example of actual gas flows revealed from images of the Hubble Space Telescope and therefore is of high scientific interest. Following the configuration in Ref. [13], we initialize the computational domain $[0, 2] \times [-0.5, 0.5]$ with the following conditions:

$$(\rho, u_x, u_y, p) = \begin{cases} (5, 11.2, 0, 0.4127), & \text{if } x = 0, -0.05 \leq y \leq 0.05 \\ (0.5, 0, 0, 0.4127), & \text{otherwise.} \end{cases} \quad (138)$$

Outflow BCs are used around the domain except the left boundary, where the prescribed fixed conditions are imposed. The simulation was performed with resolution [1200,600]. We compare the results between the $D2Q9$, $D2Q16$, and the multiscale $D2Q9$ - $D2Q16$ models. Figure 22 shows a comparison of the pressure, density and temperature fields between the $D2Q16$ and $D2Q9$ - $D2Q16$ solutions. The propagation of the bow shock into the surrounding medium as well as the developed Rayleigh Taylor instabilities within the jet cocoon are captured in very good agreement between the two simulations. Figure 23 depicts the distribution of the $D2Q16$ lattice in the computational domain. For a quantitative comparison, Fig. 24 plots the density field across three horizontal cuts of the domain. The multiscale $D2Q9$ - $D2Q16$ model and the pure $D2Q16$ are in excellent agreement. On the contrary, the pure $D2Q9$ model evolves with clear deviations, as shown in Fig. 24.

4. Shock structure problem

We revisit the shock structure problem using the $D2Q16$ and $D2Q25$ lattices. Similarly to [53], the high-order lattice is activated inside the region of the shock wave, with the refinement criterion being based on the local Knudsen number

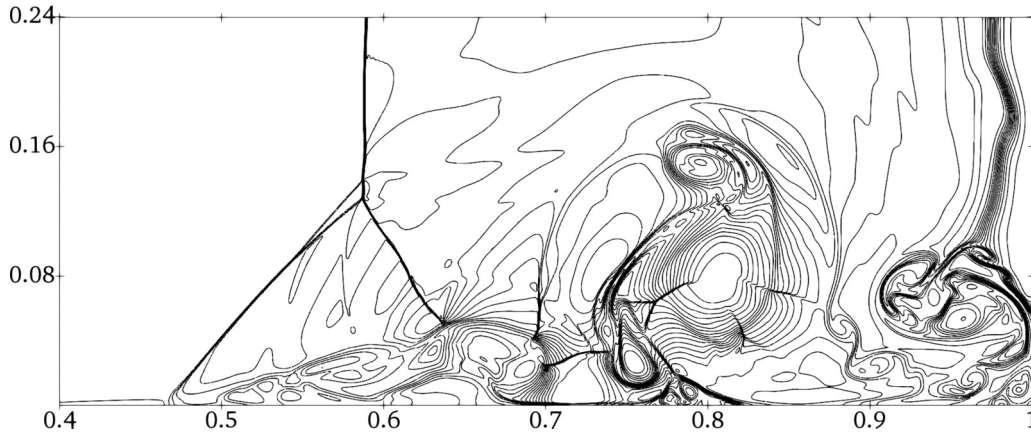


FIG. 14. Viscous shock tube problem ($Re = 1000$). Top panel shows 20 equidistant density contours $\rho \in (20, 115)$.

defined as

$$Kn = \frac{\lambda}{\left| \frac{\rho}{d\rho/dx} \right|}. \quad (139)$$

The threshold value was set to $Kn_{thr} = 0.02$, a typical value suggested in the literature [64,91]. The steady-state results for $Ma = 1.6$ are shown in Fig. 25. It is observed that the density, temperature, as well as the stress profiles match the reference results very well. Small disturbances are also recorded in the vicinity of the interface region of the different velocity sets.

5. Micro Couette flow

As a final test case, we simulate a shear driven Couette flow at a high Knudsen number. It is well known that the $D2Q9$ lattice fails to capture the Knudsen layer, resulting in significant deviations of the velocity profile [87]. Furthermore, it has been reported that even-order velocity sets perform significantly better than the odd-orders [92]. The Knudsen number in this setup can be defined as [92]

$$Kn = \frac{\mu\sqrt{T}}{pL}, \quad (140)$$

where p and L denote the pressure and the distance between sharing plates, respectively. We test the multiscale scheme with the $D2Q16$ lattice activated in the vicinity of the wall

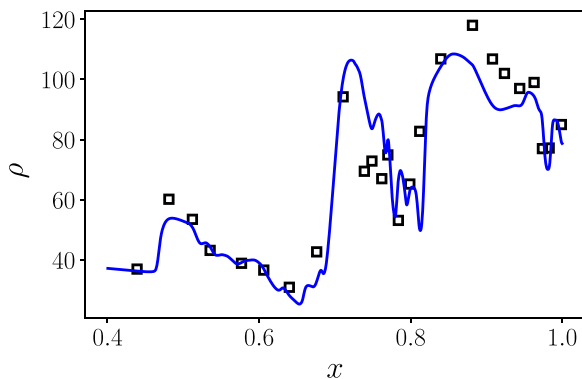


FIG. 15. Viscous shock tube problem ($Re = 1000$). Density distribution along the solid wall. Symbols show reference data from Ref. [83].

boundaries and the $D2Q9$ lattice in the main flow. The results for the nondimensional velocity (normalized with the difference of the wall velocities) for Knudsen number $Kn = 0.5$ are presented in Fig. 26, in which comparison is made with results from linearized BGK [92]. The multiscale model and the uniform $D2Q16$ solution agree very well with each other, as well as with the reference results.

E. Discussion

We summarize the main strategies that we adopted to simplify the PonD finite-volume scheme with minimal sacrifice of accuracy. The pivotal point is the identification of the frame invariant moment system for the f and g populations, according to the target hydrodynamic system. According to Sec. IID, the frame invariant moment system for the g populations should include up to second-order moments. Hence, irrespective of the f lattice, we used in all simulations in this work the $D2Q9$ lattice for the g populations, decreasing the computational cost for both the g populations update and the g reference frame transformations. Numerical experiments with different f and g lattices did not reveal any appreciable effect on the stability and the accuracy of the scheme.

The multiscale formulation enables the deployment of a low-order lattice for the f populations, in regions with smooth flow velocity and temperature variations. In accordance with observations in Ref. [53], the stability and accuracy of the solutions are well maintained. The efficiency gains from this approach are naturally case dependent. We note that the different lattices communicate solely through the Grad reference frame transformation, which renders the transition from a single lattice to a multiscale model easy to program and highly efficient.

The last element which differs from the PonD formulations in Ref. [56] is the absence of iterations within the flux calculation, as discussed in IV A 3. We demonstrate a comparison between the iterative and the current formulation through the Shu-Osher problem [90]. Figure 27 shows the results from the two schemes, for different CFL numbers and resolutions. One observes that for high CFL and coarse domains, the iterative scheme is marginally more accurate than its explicit counterpart. For moderate CFL and resolved domains the two solutions are almost indistinguishable.

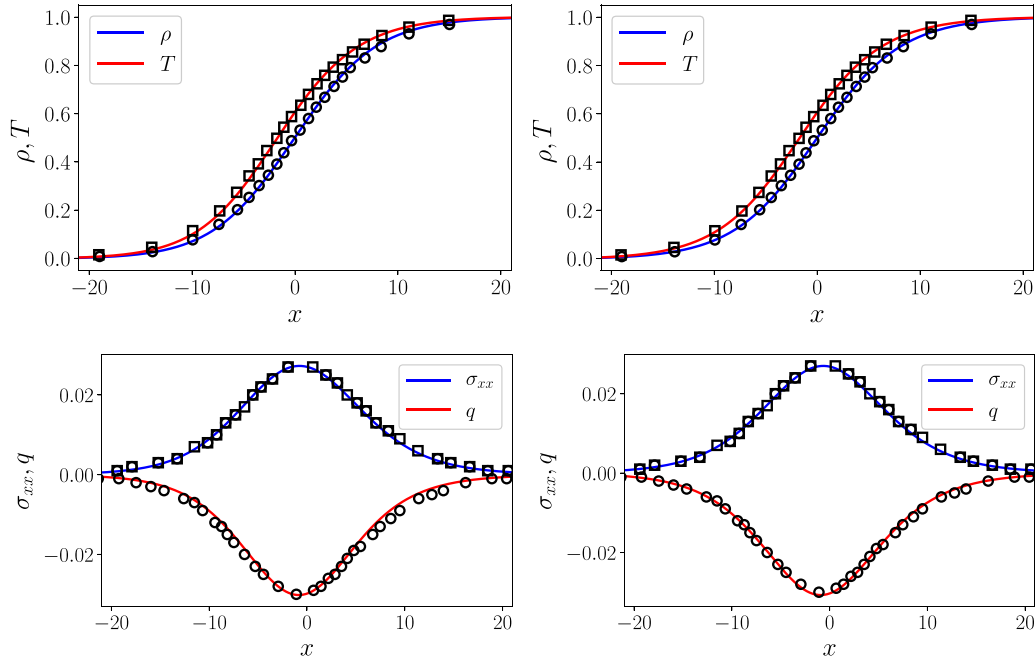


FIG. 16. The shock structure problem with Ma 1.2. Density, temperature profiles (top), normal stress and heat flux profiles (bottom). Third-order transformation in the left column, fourth-order in the right column.

Additional numerical experiments confirm the above observations. We can conclude that, for resolved simulations (spatially and temporally), the noniterative flux calculation can be safely employed.

Finally, we would like to emphasize that the properties and, more significantly, the limitations of the DUGKS method are inherent in the resulting PonD scheme. Regardless of the choice of reference frame, the linear reconstruction through

slope limiters introduces numerical dissipation, as expected from this family of schemes. Fortunately, the considerations presented in this work associated with the adaptive reference frame formulation of PonD extend beyond the confines of the specific DUGKS implementation. Combining state-of-the-art high-order and low-dissipation CFD schemes with kinetic modeling and the PonD formulation can yield promising fluid solvers capable of operating across a wide range of conditions,

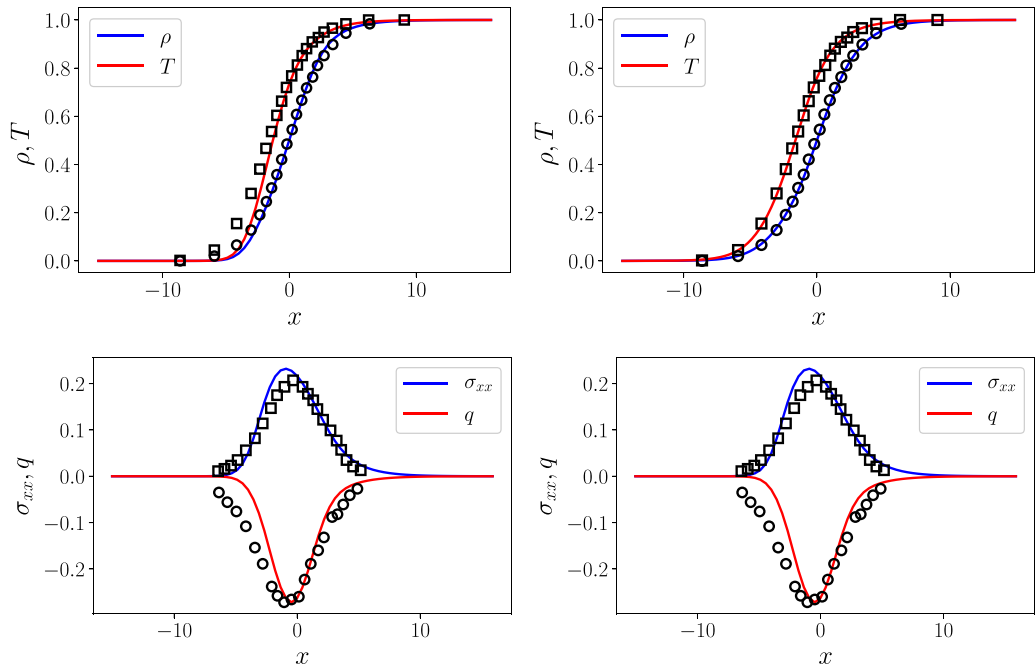


FIG. 17. The shock structure problem with Ma 1.6. Density, temperature profiles (top), normal stress and heat flux profiles (bottom). Third-order transformation at the left column, fourth-order at the right column.

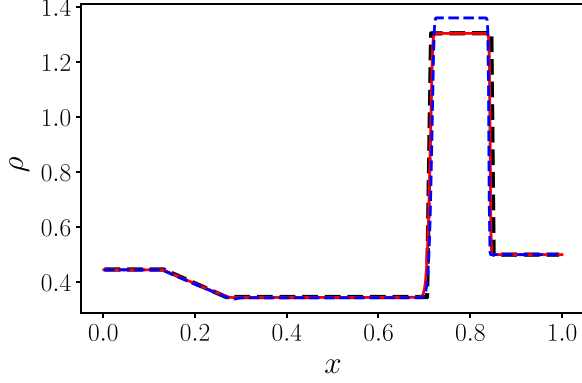


FIG. 18. Density profile for the Lax tube problem at $t = 0.14$. The red line corresponds to $D2Q16$ lattice, the blue dashed line to $D2Q9$, and the black dashed line to the analytical solution.

even in the presence of nonequilibrium phenomena. A relevant study in the context of semi-Lagrangian PonD can be found in Ref. [93].

VI. CONCLUSIONS

In this work, we presented the PonD formulation with an emphasis on the requirements of the reference frame transformation. According to the target hydrodynamic equations, conventional LBM models on a static reference frame require a set of equilibrium moment constraints. In contrast, PonD utilizes an adaptive comoving reference frame with the pertinent equilibrium moment constraints being automatically satisfied by exact equilibrium populations. However, the target hydrodynamic equations introduce requirements on the frame invariant moment system of the reference frame transformation. The framework presented in this work is a finite-volume DUGKS discretization of the governing kinetic equations in an adaptive reference frame. In comparison with the conventional DUGKS scheme, the cost to be paid for the adaptive formulation amounts to the reference frame transformations. The benefit of this approach is enhanced accuracy, stability and an increased operating window in terms of Mach number and temperature. Additionally, a multiscale extension

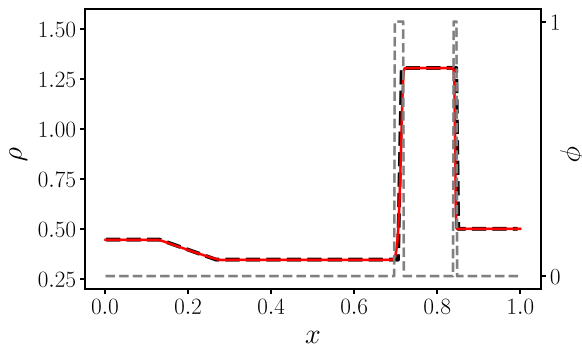


FIG. 19. Density profile for the Lax tube problem at $t = 0.14$. The red line corresponds to the $D2Q9$ - $D2Q16$ model and the black dashed line to the analytical solution. The gray dashed line indicates the occupancy regions of the $D2Q16$ lattice ($\phi = 1$) and of the $D2Q9$ lattice ($\phi = 0$).

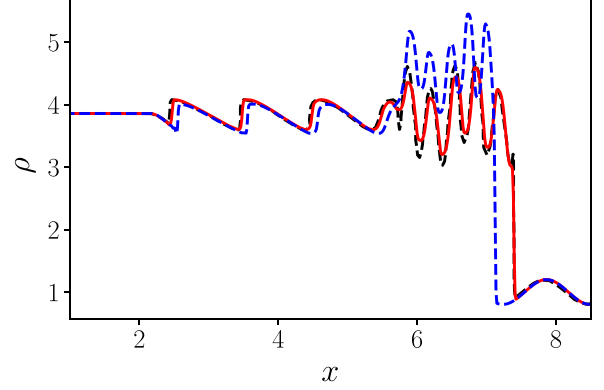


FIG. 20. Density profile for the Shu-Osher problem at $t = 1.8$. The red line corresponds to the $D2Q16$ lattice, the blue dashed line to the $D2Q9$, and the black dashed line to the reference solution [90].

can easily be incorporated and results in further efficiency gains. Further high Mach three-dimensional simulations with the presence of curved boundaries shall be the focus of future work.

ACKNOWLEDGMENTS

This work was supported by European Research Council (ERC) Advanced Grant No. 834763-PonD. Computational resources at the Swiss National Super Computing Center CSCS were provided under the Grants No. s1066 and No. s1222.

APPENDIX A: HERMITE POLYNOMIALS

The Hermite polynomials up to fourth order and with discrete velocities scaled such that $T_L = 1$ are the following:

$$H_i^{(0)} = 1, \quad (\text{A1})$$

$$H_{i\alpha}^{(1)} = c_{i\alpha}, \quad (\text{A2})$$

$$H_{i\alpha\beta}^{(2)} = c_{i\alpha}c_{i\beta} - \delta_{\alpha\beta}, \quad (\text{A3})$$

$$H_{i\alpha\beta\gamma}^{(3)} = c_{i\alpha}c_{i\beta}c_{i\gamma} - [c_{i\alpha}\delta_{\beta\gamma}]_{\text{cyc}}, \quad (\text{A4})$$

$$H_{i\alpha\beta\gamma\delta}^{(4)} = c_{i\alpha}c_{i\beta}c_{i\gamma}c_{i\delta} - [c_{i\alpha}c_{i\beta}\delta_{\gamma\delta}]_{\text{cyc}} + [\delta_{\alpha\beta}\delta_{\gamma\delta}]_{\text{cyc}}, \quad (\text{A5})$$

where $[\]_{\text{cyc}}$ stands for cyclic permutations without repetition over indices. The contracted fourth-order polynomial is the following:

$$H_{i,\alpha\beta}^{(4)} = c_{i\alpha}c_{i\beta} [c_i^2 - (D+4)] - \delta_{\alpha\beta} [c_i^2 - (D+2)]. \quad (\text{A6})$$

Calculation of expansion coefficients for given moments $\mathbf{m} = \{M^{(0)}, M_\alpha^{(1)}, M_{\alpha\beta}^{(2)}, M_{\alpha\beta\gamma}^{(3)}, M_{\alpha\beta\gamma\delta}^{(4)}\}$ and target reference frame $\lambda = \{T, \mathbf{u}\}$. The population in the target reference frame is expanded in Grad series,

$$f_i^\lambda = W_i \sum_{n=0}^4 \frac{1}{n!} \alpha^{(n)}(\mathbf{m}; \lambda) H^{(n)}(\mathbf{c}_i). \quad (\text{A7})$$

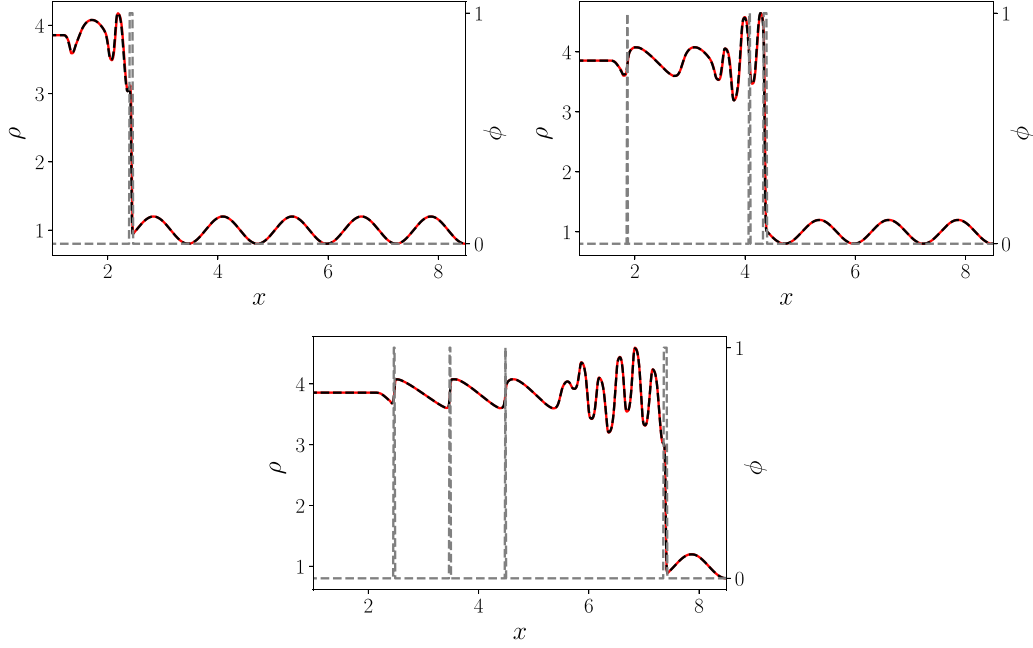


FIG. 21. Density profile for the Shu-Osher problem at different times. The red line corresponds to the $D2Q9$ - $D2Q16$ model and the black dashed line to the $D2Q16$ solution. The gray dashed line indicates the occupancy regions of the $D2Q16$ lattice ($\phi = 1$) and of the $D2Q9$ lattice ($\phi = 0$).

The constraints which enforce the reference frame invariance of the selected moments are

$$M^{(0)} = \sum_{i=0}^{Q-1} f_i^\lambda, \quad (\text{A8})$$

$$M_\alpha^{(1)} = \sum_{i=0}^{Q-1} f_i^\lambda v_{i\alpha}^\lambda, \quad (\text{A9})$$

$$M_{\alpha\beta}^{(2)} = \sum_{i=0}^{Q-1} f_i^\lambda v_{i\alpha}^\lambda v_{i\beta}^\lambda, \quad (\text{A10})$$

$$M_{\alpha\beta\gamma}^{(3)} = \sum_{i=0}^{Q-1} f_i^\lambda v_{i\alpha}^\lambda v_{i\beta}^\lambda v_{i\gamma}^\lambda, \quad (\text{A11})$$

$$M_{\alpha\beta}^{(4)} = \sum_{i=0}^{Q-1} f_i^\lambda v_{i\alpha}^\lambda v_{i\beta}^\lambda v_{i\gamma}^\lambda v_{i\gamma}^\lambda, \quad (\text{A12})$$

where the discrete velocities are $v_{i\alpha}^\lambda = (\sqrt{T}c_{i\alpha} + u_\alpha)$. The solution for the expansion coefficients is

$$\alpha^{(0)} = M^{(0)}, \quad (\text{A13})$$

$$\alpha_\alpha^{(1)} = \frac{1}{T^{1/2}} (M_\alpha^{(1)} - u_\alpha M^{(0)}), \quad (\text{A14})$$

$$\alpha_{\alpha\beta}^{(2)} = \frac{1}{T} \{ M_{\alpha\beta}^{(2)} - M^{(0)} (T\delta_{\alpha\beta} - u_\alpha u_\beta M^{(0)}) - [u_\alpha (M_\beta^{(1)} - u_\beta M^{(0)})]_{\text{cyc}} \}, \quad (\text{A15})$$

$$\alpha_{\alpha\beta\gamma}^{(3)} = \frac{1}{T^{3/2}} \{ M_{\alpha\beta\gamma}^{(3)} - u_\alpha u_\beta u_\gamma M^{(0)} - [(M_\alpha^{(1)} - M^{(0)} u_\alpha) (T\delta_{\beta\gamma} - u_\beta u_\gamma)]_{\text{cyc}} - [(M_{\alpha\beta}^{(2)} - M^{(0)} u_\alpha u_\beta) u_\gamma]_{\text{cyc}} \}. \quad (\text{A16})$$

APPENDIX B: PARTICLES ON DEMAND EQUATION

We start with the kinetic equation formulated at a constant, uniform monitoring reference frame $\bar{\lambda}$,

$$\partial_t f_i^{\bar{\lambda}} + \mathbf{v}_i^{\bar{\lambda}} \cdot \nabla f_i^{\bar{\lambda}} = \Omega_i^{\bar{\lambda}}. \quad (\text{B1})$$

The moments $\mathbf{m}^{\bar{\lambda}}$ at the monitoring frame $\bar{\lambda}$ are connected with the corresponding populations via a linear matrix $\mathcal{M}^{\bar{\lambda}}$,

$$\mathbf{m}_i^{\bar{\lambda}} = \mathcal{M}_{i,j}^{\bar{\lambda}} f_j^{\bar{\lambda}}, \quad (\text{B2})$$

$$f_i^{\bar{\lambda}} = [\mathcal{M}^{\bar{\lambda}}]_{i,j}^{-1} \mathbf{m}_j^{\bar{\lambda}}. \quad (\text{B3})$$

We insert Eq. (B3) into Eq. (B1) and obtain the following equation:

$$\partial_t ([\mathcal{M}^{\bar{\lambda}}]_{i,j}^{-1} \mathbf{m}_j^{\bar{\lambda}}) + \mathbf{v}_i^{\bar{\lambda}} \cdot \nabla ([\mathcal{M}^{\bar{\lambda}}]_{i,j}^{-1} \mathbf{m}_j^{\bar{\lambda}}) = [\mathcal{M}^{\bar{\lambda}}]_{i,j}^{-1} \mathbf{m}_{\Omega,j}^{\bar{\lambda}}, \quad (\text{B4})$$

where $\mathbf{m}_{\Omega,j}^{\bar{\lambda}}$ denotes the moments from the collision operator. Next, we invoke the reference frame invariance of the moments,

$$\mathbf{m}_i^{\bar{\lambda}} = m_i^{\lambda(x,t)}, \quad (\text{B5})$$

where $\lambda(x, t)$ denotes the local reference frame. We insert the moments evaluated from the local reference frame (B5) into Eq. (B4),

$$\begin{aligned} \partial_t ([\mathcal{M}^{\bar{\lambda}}]_{i,j}^{-1} m_j^{\lambda(x,t)}) + \mathbf{v}_i^{\bar{\lambda}} \cdot \nabla ([\mathcal{M}^{\bar{\lambda}}]_{i,j}^{-1} m_j^{\lambda(x,t)}) \\ = [\mathcal{M}^{\bar{\lambda}}]_{i,j}^{-1} m_{\Omega,j}^{\lambda(x,t)}. \end{aligned} \quad (\text{B6})$$

Subsequently, we interchange the moments $m_j^{\lambda(x,t)}$ with their populations at the local reference frame,

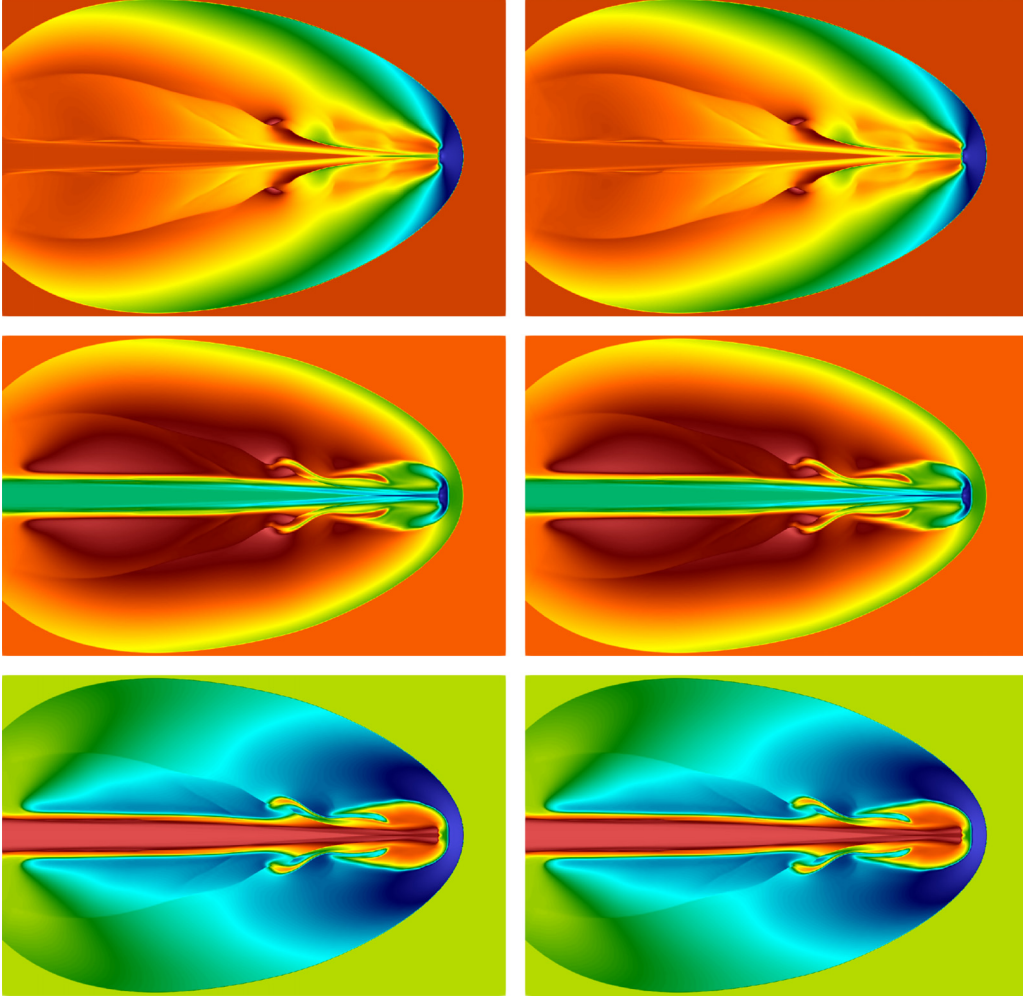


FIG. 22. Mach 30 astrophysical jet problem. Top panel shows pressure $p \in (0.4, 305)$, middle panel shows density $\rho \in (0.1, 42)$, bottom panel shows temperature $T \in (0.1, 105)$. Left column shows $D2Q16$. Right column shows $D2Q9$ - $D2Q16$.

$$m_j^{\lambda(x,t)} = \mathcal{M}_{j,k}^{\lambda(x,t)} f_k^{\lambda(x,t)} \text{ and retrieve the following equation:}$$

$$\partial_t ([\mathcal{M}_{i,j}^{\bar{\lambda}}]^{-1} \mathcal{M}_{j,k}^{\lambda(x,t)} f_k^{\lambda(x,t)}) + \mathbf{v}_i^{\bar{\lambda}} \cdot \nabla ([\mathcal{M}_{i,j}^{\bar{\lambda}}]^{-1} \mathcal{M}_{j,k}^{\lambda(x,t)} f_k^{\lambda(x,t)}) = [\mathcal{M}_{i,j}^{\bar{\lambda}}]^{-1} \mathcal{M}_{j,k}^{\lambda(x,t)} \Omega_k^{\lambda(x,t)}. \quad (\text{B7})$$

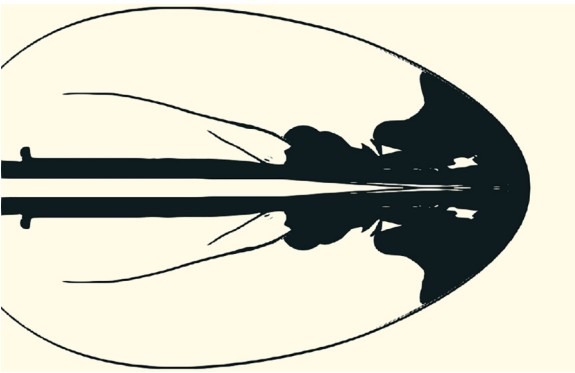


FIG. 23. Mach 30 astrophysical jet problem. Lattice distribution for the $D2Q9$ - $D2Q16$ model. Black regions indicate the $D2Q16$ lattice.

The multiplication of the matrices $[\mathcal{M}_{i,j}^{\bar{\lambda}}]^{-1} \mathcal{M}_{j,k}^{\lambda(x,t)}$ is the definition of the reference frame transformation,

$$[\mathcal{G}_{\lambda(x,t)}^{\bar{\lambda}}]_{i,k} = [\mathcal{M}_{i,j}^{\bar{\lambda}}]^{-1} \mathcal{M}_{j,k}^{\lambda(x,t)}, \quad (\text{B8})$$

from the local frame $\lambda(x, t)$ to the monitoring frame $\bar{\lambda}$. Thus, Eq. (B7) is the final PonD equation,

$$\partial_t (\mathcal{G}_{i,\lambda(x,t)}^{\bar{\lambda}} f^{\lambda(x,t)}) + \mathbf{v}_i^{\bar{\lambda}} \cdot \nabla (\mathcal{G}_{i,\lambda(x,t)}^{\bar{\lambda}} f^{\lambda(x,t)}) = \mathcal{G}_{i,\lambda(x,t)}^{\bar{\lambda}} \Omega^{\lambda(x,t)}, \quad (\text{B9})$$

where, for convenience, the summation over repeated indices is not explicit,

$$\mathcal{G}_{i,\lambda(x,t)}^{\bar{\lambda}} f^{\lambda(x,t)} = [\mathcal{G}_{\lambda(x,t)}^{\bar{\lambda}}]_{i,k} f_k^{\lambda(x,t)}. \quad (\text{B10})$$

APPENDIX C: CONSERVATION PROPERTIES

Without loss of generality, we consider a face at x_I , with a unit normal vector pointing at the x direction. According to the presented scheme, the fluxes have been calculated with a

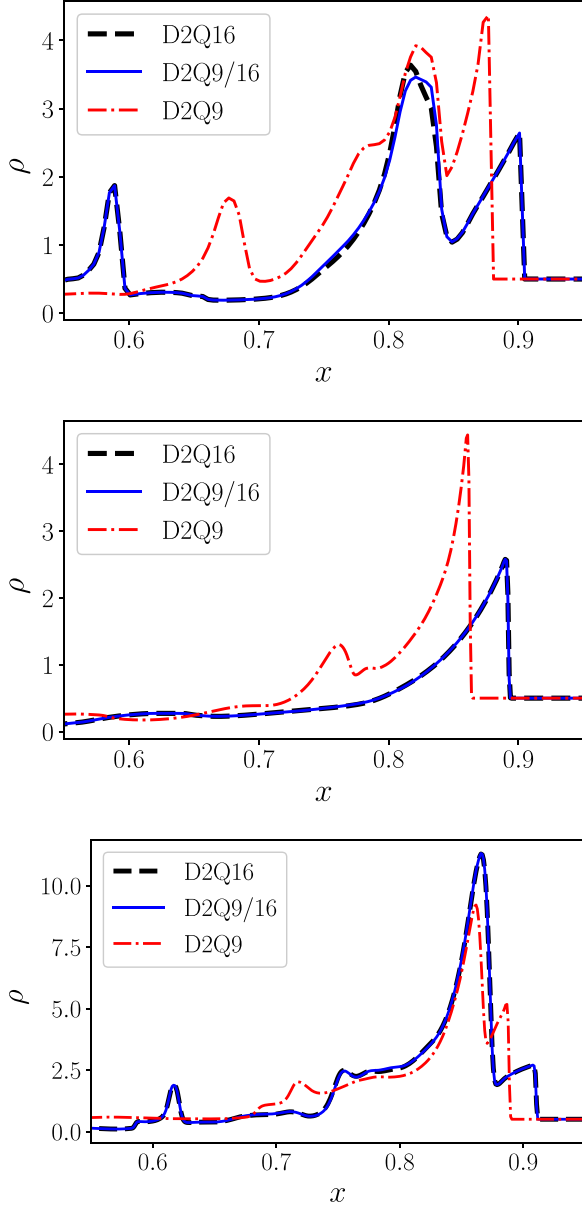


FIG. 24. Mach 30 astrophysical jet problem. Density profiles of the $D2Q16$ (black dashed line), $D2Q9$ (red dashed dotted line), and $D2Q9$ - $D2Q16$ (blue solid line) models, across horizontal cuts of the domain. The horizontal cuts intercept the y axis at $y/L_y = 0.66$ (top), $y/L_y = 0.7$ (middle), and $y/L_y = 0.73$ (bottom).

reference frame $\bar{\lambda}$ and are calculated as

$$F_{f,i}^{\bar{\lambda}}(\mathbf{x}_I) = v_{ix}^{\bar{\lambda}} f_i^{\bar{\lambda}}(\mathbf{x}_I), \quad (C1)$$

$$F_{g,i}^{\bar{\lambda}}(\mathbf{x}_I) = v_{ix}^{\bar{\lambda}} g_i^{\bar{\lambda}}(\mathbf{x}_I). \quad (C2)$$

The f populations at the left and right neighboring cells \mathbf{x}_L , \mathbf{x}_R are updated due to the fluxes $F_{f,i}^{\bar{\lambda}}(\mathbf{x}_I)$ as

$$f_i^{\lambda_L}(\mathbf{x}_L, t_{n+1}) = f_i^{\lambda_L}(\mathbf{x}_L, t_n) - \delta t \mathcal{G}_{i,\bar{\lambda}}^{\lambda_L} F_{f,i}^{\bar{\lambda}}(\mathbf{x}_I), \quad (C3)$$

$$f_i^{\lambda_R}(\mathbf{x}_R, t_{n+1}) = f_i^{\lambda_R}(\mathbf{x}_R, t_n) + \delta t \mathcal{G}_{i,\bar{\lambda}}^{\lambda_R} F_{f,i}^{\bar{\lambda}}(\mathbf{x}_I), \quad (C4)$$

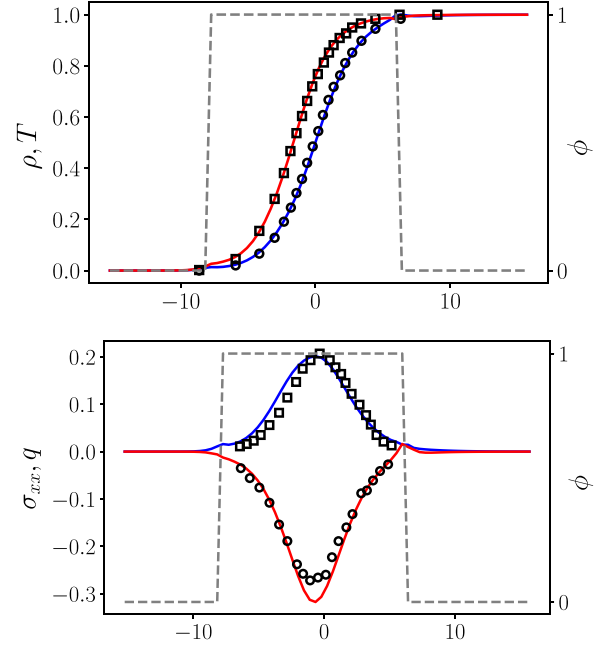


FIG. 25. The shock structure problem with the multiscale framework at $Ma = 1.6$. Top panel shows the density and temperature profiles. Bottom panel shows the normal stresses and heat flux. Comparison with the results of Ohwada [86]. $\phi = 1$ indicates the $D2Q25$ lattice and $\phi = 0$ the $D2Q16$ lattice.

and accordingly the g populations

$$g_i^{\lambda_L}(\mathbf{x}_L, t_{n+1}) = g_i^{\lambda_L}(\mathbf{x}_L, t_n) - \delta t \mathcal{G}_{i,\bar{\lambda}}^{\lambda_L} F_g^{\bar{\lambda}}(\mathbf{x}_I), \quad (C5)$$

$$g_i^{\lambda_R}(\mathbf{x}_R, t_{n+1}) = g_i^{\lambda_R}(\mathbf{x}_R, t_n) + \delta t \mathcal{G}_{i,\bar{\lambda}}^{\lambda_R} F_g^{\bar{\lambda}}(\mathbf{x}_I). \quad (C6)$$

By summing over the population, we obtain the updates of the mass, momentum, and energy at the left $\delta\rho_L$, $\delta(\rho\mathbf{u})_L$, $\delta(\rho E)_L$ and right $\delta\rho_R$, $\delta(\rho\mathbf{u})_R$, $\delta(\rho E)_R$ neighboring cells due to the

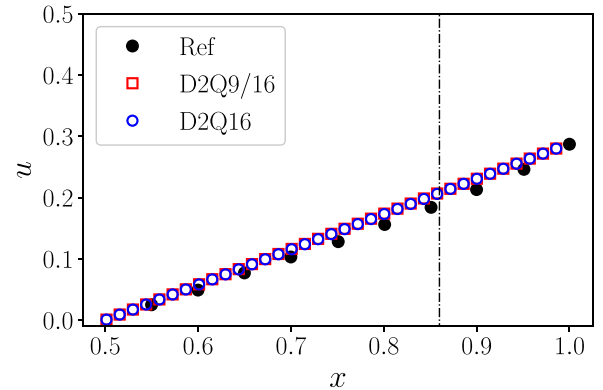


FIG. 26. Normalized velocity for the shear driven Couette flow with the $D2Q9$ - $D2Q16$ multiscale framework, at Knudsen number equal to 0.5. The vertical dotted line indicates the interface of the different velocity sets. The $D2Q16$ lattice is activated in the vicinity of the walls, while the $D2Q9$ everywhere else. The reference results are obtained from Ref. [64].

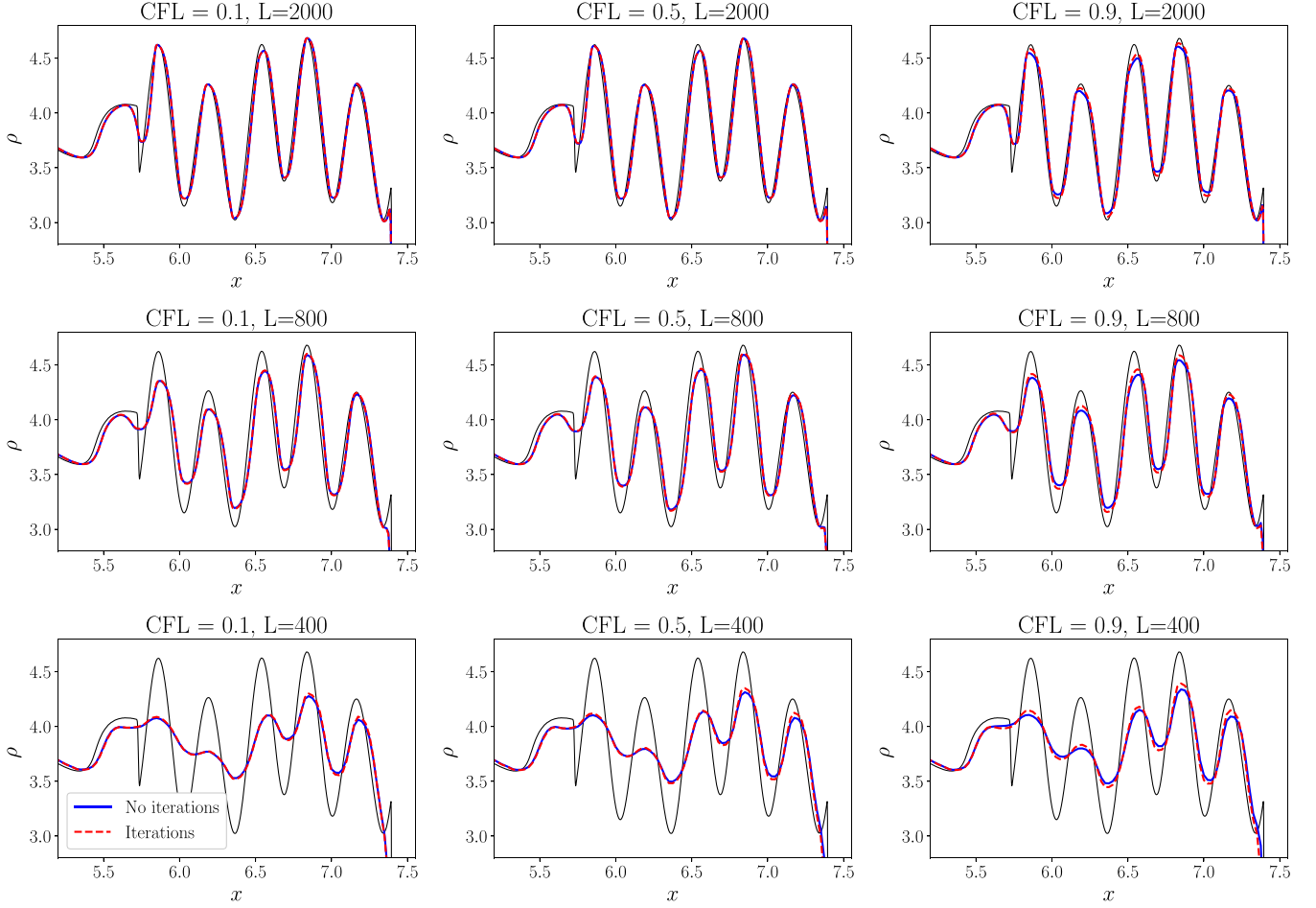


FIG. 27. Density profile for the Shu-Osher problem, comparing the scheme with (red dashed line) and without (blue solid line) iterations. Black solid line corresponds to the reference results [90]. Results are shown for different CFL numbers and resolution.

fluxes of the interface,

$$\delta \rho_L = \sum_{i=0}^{Q-1} \{f_i^{\lambda_L}(\mathbf{x}_L, t_{n+1}) - f_i^{\lambda_L}(\mathbf{x}_L, t_n)\} = -\delta t \sum_{i=0}^{Q-1} \mathcal{G}_{i,\bar{\lambda}}^{\lambda_L} F_f^{\bar{\lambda}}(\mathbf{x}_I), \quad (\text{C7})$$

$$\delta(\rho \mathbf{u})_L = \sum_{i=0}^{Q-1} \{v_i^{\lambda_L} f_i^{\lambda_L}(\mathbf{x}_L, t_{n+1}) - v_i^{\lambda_L} f_i^{\lambda_L}(\mathbf{x}_L, t_n)\} = -\delta t \sum_{i=0}^{Q-1} v_i^{\lambda_L} \mathcal{G}_{i,\bar{\lambda}}^{\lambda_L} F_f^{\bar{\lambda}}(\mathbf{x}_I), \quad (\text{C8})$$

$$\begin{aligned} \delta(\rho E)_L &= \sum_{i=0}^{Q-1} \left\{ \frac{(v_i^{\lambda_L})^2}{2} f_i^{\lambda_L}(\mathbf{x}_L, t_{n+1}) + g_i^{\lambda_L}(\mathbf{x}_L, t_{n+1}) - \frac{(v_i^{\lambda_L})^2}{2} f_i^{\lambda_L}(\mathbf{x}_L, t_n) - g_i^{\lambda_L}(\mathbf{x}_L, t_n) \right\} \\ &= -\delta t \sum_{i=0}^{Q-1} \left\{ \frac{(v_i^{\lambda_L})^2}{2} \mathcal{G}_{i,\bar{\lambda}}^{\lambda_L} F_f^{\bar{\lambda}}(\mathbf{x}_I) + \mathcal{G}_{i,\bar{\lambda}}^{\lambda_L} F_g^{\bar{\lambda}}(\mathbf{x}_I) \right\}, \end{aligned} \quad (\text{C9})$$

$$\delta \rho_R = \sum_{i=0}^{Q-1} \{f_i^{\lambda_R}(\mathbf{x}_R, t_{n+1}) - f_i^{\lambda_R}(\mathbf{x}_R, t_n)\} = \delta t \sum_{i=0}^{Q-1} \mathcal{G}_{i,\bar{\lambda}}^{\lambda_R} F_f^{\bar{\lambda}}(\mathbf{x}_I), \quad (\text{C10})$$

$$\delta(\rho \mathbf{u})_R = \sum_{i=0}^{Q-1} \{v_i^{\lambda_R} f_i^{\lambda_R}(\mathbf{x}_R, t_{n+1}) - v_i^{\lambda_R} f_i^{\lambda_R}(\mathbf{x}_R, t_n)\} = \delta t \sum_{i=0}^{Q-1} v_i^{\lambda_R} \mathcal{G}_{i,\bar{\lambda}}^{\lambda_R} F_f^{\bar{\lambda}}(\mathbf{x}_I), \quad (\text{C11})$$

$$\begin{aligned} \delta(\rho E)_R &= \sum_{i=0}^{Q-1} \left\{ \frac{(v_i^{\lambda_R})^2}{2} f_i^{\lambda_R}(\mathbf{x}_R, t_{n+1}) + g_i^{\lambda_R}(\mathbf{x}_R, t_{n+1}) - \frac{(v_i^{\lambda_R})^2}{2} f_i^{\lambda_R}(\mathbf{x}_R, t_n) - g_i^{\lambda_R}(\mathbf{x}_R, t_n) \right\} \\ &= \delta t \sum_{i=0}^{Q-1} \left\{ \frac{(v_i^{\lambda_R})^2}{2} \mathcal{G}_{i,\bar{\lambda}}^{\lambda_R} F_f^{\bar{\lambda}}(\mathbf{x}_I) + \mathcal{G}_{i,\bar{\lambda}}^{\lambda_R} F_g^{\bar{\lambda}}(\mathbf{x}_I) \right\}. \end{aligned} \quad (\text{C12})$$

The finite volume is strictly conservative with respect to mass, momentum, and total energy when

$$\delta\rho_R + \delta\rho_L = 0, \quad (C13)$$

$$\delta(\rho\mathbf{u})_R + \delta(\rho\mathbf{u})_L = 0, \quad (C14)$$

$$\delta(\rho E)_R + \delta(\rho E)_L = 0. \quad (C15)$$

Substituting from the above expressions we arrive at the following constraints:

$$\sum_{i=0}^{Q-1} \mathcal{G}_{i,\bar{\lambda}}^{\lambda_L} F_f^{\bar{\lambda}} = \sum_{i=0}^{Q-1} \mathcal{G}_{i,\bar{\lambda}}^{\lambda_R} F_f^{\bar{\lambda}}, \quad (C16)$$

$$\sum_{i=0}^{Q-1} \mathbf{v}_i^{\lambda_L} \mathcal{G}_{i,\bar{\lambda}}^{\lambda_L} F_f^{\bar{\lambda}} = \sum_{i=0}^{Q-1} \mathbf{v}_i^{\lambda_R} \mathcal{G}_{i,\bar{\lambda}}^{\lambda_R} F_f^{\bar{\lambda}}, \quad (C17)$$

$$\sum_{i=0}^{Q-1} \frac{(\mathbf{v}_i^{\lambda_L})^2}{2} \mathcal{G}_{i,\bar{\lambda}}^{\lambda_L} F_f^{\bar{\lambda}} + \mathcal{G}_{i,\bar{\lambda}}^{\lambda_L} F_g^{\bar{\lambda}} = \sum_{i=0}^{Q-1} \frac{(\mathbf{v}_i^{\lambda_R})^2}{2} \mathcal{G}_{i,\bar{\lambda}}^{\lambda_R} F_f^{\bar{\lambda}} + \mathcal{G}_{i,\bar{\lambda}}^{\lambda_R} F_g^{\bar{\lambda}}. \quad (C18)$$

The constraints are satisfied if the following moments of the f populations are invariant upon reference frame transformation,

$$\sum_{i=0}^{Q-1} v_{ix}^{\lambda_L} f_i^{\lambda_L} = \sum_{i=0}^{Q-1} v_{ix}^{\lambda_R} f_i^{\lambda_R}, \quad (C19)$$

$$\sum_{i=0}^{Q-1} \mathbf{v}_i^{\lambda_L} v_{ix}^{\lambda_L} f_i^{\lambda_L} = \sum_{i=0}^{Q-1} \mathbf{v}_i^{\lambda_R} v_{ix}^{\lambda_R} f_i^{\lambda_R}, \quad (C20)$$

$$\sum_{i=0}^{Q-1} (\mathbf{v}_i^{\lambda_L})^2 v_{ix}^{\lambda_L} f_i^{\lambda_L} = \sum_{i=0}^{Q-1} (\mathbf{v}_i^{\lambda_R})^2 v_{ix}^{\lambda_R} f_i^{\lambda_R}, \quad (C21)$$

and the following for the g populations,

$$\sum_{i=0}^{Q-1} v_{ix}^{\lambda_L} g_i^{\lambda_L} = \sum_{i=0}^{Q-1} v_{ix}^{\lambda_R} g_i^{\lambda_R}. \quad (C22)$$

APPENDIX D: FORCING SCHEME

We consider the continuous kinetic equation with a forcing term

$$\partial_t f_i + \mathbf{v}_i \cdot \nabla f_i = \frac{1}{\tau} (f_i^{\text{eq}} - f_i) + F_i. \quad (D1)$$

The body force can be expressed as

$$F_i = -\frac{\mathbf{a} \cdot (\mathbf{v}_i - \mathbf{u})}{T} f_i^{\text{eq}}. \quad (D2)$$

The force can be incorporated by the Strang-Splitting approach,

$$\partial_t f_i = F_i \text{ (for } \delta t/2), \quad (D3)$$

$$\partial_t f_i + \mathbf{v}_i \cdot \nabla f_i = \frac{1}{\tau} (f_i^{\text{eq}} - f_i) \text{ (for } \delta t), \quad (D4)$$

$$\partial_t f_i = F_i \text{ (for } \delta t/2). \quad (D5)$$

The intermediate step is the kinetic update without body force. In the two half-time forcing steps, the distribution function and the macroscopic velocity are updated as

$$f_i^* = f_i + \frac{1}{2} \delta t F_i, \quad (D6)$$

$$\mathbf{u}^* = \mathbf{u} + \frac{1}{2} \delta t \mathbf{a}. \quad (D7)$$

-
- [1] Y. Ha and C. L. Gardner, Positive scheme numerical simulation of high Mach number astrophysical jets, *J. Sci. Comput* **34**, 247 (2008).
 - [2] C. L. Gardner and S. J. Dwyer, Numerical simulation of the XZ Tauri supersonic astrophysical jet, *Acta Math. Sci.* **29**, 1677 (2009).
 - [3] J. Urzay, Supersonic combustion in air-breathing propulsion systems for hypersonic flight, *Annu. Rev. Fluid Mech.* **50**, 593 (2018).
 - [4] J. Von Neumann and R. D. Richtmyer, A method for the numerical calculation of hydrodynamic shocks, *J. Appl. Phys.* **21**, 232 (1950).
 - [5] A. Harten, High resolution schemes for hyperbolic conservation laws, *J. Comput. Phys.* **49**, 357 (1983).
 - [6] A. Harten and S. Osher, Uniformly high-order accurate nonoscillatory schemes. I, *SIAM J. Numer. Anal.* **24**, 279 (1987).
 - [7] A. Harten, B. Engquist, S. Osher, and S. R. Chakravarthy, Uniformly high order accurate essentially non-oscillatory schemes, III, *J. Comput. Phys.* **71**, 231 (1987).
 - [8] X.-D. Liu, S. Osher, and T. Chan, Weighted essentially non-oscillatory schemes, *J. Comput. Phys.* **115**, 200 (1994).
 - [9] G.-S. Jiang and C.-W. Shu, Efficient implementation of weighted ENO schemes, *J. Comput. Phys.* **126**, 202 (1996).
 - [10] S. Pirozzoli, Numerical methods for high-speed flows, *Annu. Rev. Fluid Mech.* **43**, 163 (2011).
 - [11] J. A. Ekaterinaris, High-order accurate, low numerical diffusion methods for aerodynamics, *Prog. Aerosp. Sci.* **41**, 192 (2005).
 - [12] L. Fu, X. Y. Hu, and N. A. Adams, A family of high-order targeted ENO schemes for compressible-fluid simulations, *J. Comput. Phys.* **305**, 333 (2016).
 - [13] X. Zhang and C.-W. Shu, On positivity-preserving high order discontinuous Galerkin schemes for compressible Euler equations on rectangular meshes, *J. Comput. Phys.* **229**, 8918 (2010).
 - [14] L. Fu, A very-high-order TENO scheme for all-speed gas dynamics and turbulence, *Comput. Phys. Commun.* **244**, 117 (2019).

- [15] X. Zhang and C.-W. Shu, Positivity-preserving high order finite difference WENO schemes for compressible Euler equations, *J. Comput. Phys.* **231**, 2245 (2012).
- [16] B. Dorschner, S. S. Chikatamarla, and I. V. Karlin, Transitional flows with the entropic lattice Boltzmann method, *J. Fluid Mech.* **824**, 388 (2017).
- [17] B. Dorschner, F. Bösch, S. S. Chikatamarla, K. Boulouchos, and I. V. Karlin, Entropic multi-relaxation time lattice Boltzmann model for complex flows, *J. Fluid Mech.* **801**, 623 (2016).
- [18] X. He, S. Chen, and G. D. Doolen, A novel thermal model for the lattice Boltzmann method in incompressible limit, *J. Comput. Phys.* **146**, 282 (1998).
- [19] Z. Guo, C. Zheng, B. Shi, and T. S. Zhao, Thermal lattice Boltzmann equation for low Mach number flows: Decoupling model, *Phys. Rev. E* **75**, 036704 (2007).
- [20] I. V. Karlin, D. Sichau, and S. S. Chikatamarla, Consistent two-population lattice Boltzmann model for thermal flows, *Phys. Rev. E* **88**, 063310 (2013).
- [21] A. Mazloomi M., S. S. Chikatamarla, and I. V. Karlin, Entropic lattice Boltzmann method for multiphase flows, *Phys. Rev. Lett.* **114**, 174502 (2015).
- [22] A. M. Mazloomi, S. S. Chikatamarla, and I. V. Karlin, Drops bouncing off macro-textured superhydrophobic surfaces, *J. Fluid Mech.* **824**, 866 (2017).
- [23] M. Wöhrwag, C. Semperebon, A. Mazloomi Moqaddam, I. Karlin, and H. Kusumaatmaja, Ternary free-energy entropic lattice Boltzmann model with a high density ratio, *Phys. Rev. Lett.* **120**, 234501 (2018).
- [24] N. Sawant, B. Dorschner, and I. V. Karlin, Consistent lattice Boltzmann model for multicomponent mixtures, *J. Fluid Mech.* **909**, A1 (2021).
- [25] N. Sawant, B. Dorschner, and I. V. Karlin, A lattice Boltzmann model for reactive mixtures, *Philos. Trans. R. Soc., A* **379**, 20200402 (2021).
- [26] X. Shan, X.-F. Yuan, and H. Chen, Kinetic theory representation of hydrodynamics: A way beyond the Navier–Stokes equation, *J. Fluid Mech.* **550**, 413 (2006).
- [27] K. V. Sharma, R. Straka, and F. W. Tavares, Current status of lattice Boltzmann methods applied to aerodynamic, aeroacoustic, and thermal flows, *Prog. Aerosp. Sci.* **115**, 100616 (2020).
- [28] T. Krueger, H. Kusumaatmaja, A. Kuzmin, O. Shardt, G. Silva, and E. Vigen, *The Lattice Boltzmann Method: Principles and Practice*, Graduate Texts in Physics (Springer, Berlin, 2016).
- [29] S. Succi, *The Lattice Boltzmann Equation: For Complex States of Flowing Matter* (Oxford University Press, Oxford, 2018).
- [30] Y. H. Qian and S. A. Orszag, Lattice BGK models for the Navier-Stokes equation: Nonlinear deviation in compressible regimes, *Europhys. Lett.* **21**, 255 (1993).
- [31] G. R. McNamara, A. L. Garcia, and B. J. Alder, Stabilization of thermal lattice Boltzmann models, *J. Stat. Phys.* **81**, 395 (1995).
- [32] X. Shan and X. He, Discretization of the velocity space in the solution of the Boltzmann equation, *Phys. Rev. Lett.* **80**, 65 (1998).
- [33] N. I. Prasianakis and I. V. Karlin, Lattice Boltzmann method for thermal flow simulation on standard lattices, *Phys. Rev. E* **76**, 016702 (2007).
- [34] M. H. Saadat, F. Bösch, and I. V. Karlin, Lattice Boltzmann model for compressible flows on standard lattices: Variable Prandtl number and adiabatic exponent, *Phys. Rev. E* **99**, 013306 (2019).
- [35] M. H. Saadat, B. Dorschner, and I. Karlin, Extended lattice Boltzmann model, *Entropy* **23**, 475 (2021).
- [36] M. H. Saadat, S. A. Hosseini, B. Dorschner, and I. V. Karlin, Extended lattice Boltzmann model for gas dynamics, *Phys. Fluids* **33**, 046104 (2021).
- [37] S. S. Chikatamarla and I. V. Karlin, Entropy and Galilean invariance of lattice Boltzmann theories, *Phys. Rev. Lett.* **97**, 190601 (2006).
- [38] S. S. Chikatamarla and I. V. Karlin, Lattices for the lattice Boltzmann method, *Phys. Rev. E* **79**, 046701 (2009).
- [39] F. J. Alexander, S. Chen, and J. D. Sterling, Lattice Boltzmann thermohydrodynamics, *Phys. Rev. E* **47**, R2249(R) (1993).
- [40] N. Frapolli, S. S. Chikatamarla, and I. V. Karlin, Entropic lattice Boltzmann model for compressible flows, *Phys. Rev. E* **92**, 061301(R) (2015).
- [41] N. Frapolli, S. S. Chikatamarla, and I. V. Karlin, Entropic lattice Boltzmann model for gas dynamics: Theory, boundary conditions, and implementation, *Phys. Rev. E* **93**, 063302 (2016).
- [42] Y. Feng, P. Sagaut, and W.-Q. Tao, A compressible lattice Boltzmann finite-volume model for high subsonic and transonic flows on regular lattices, *Comput. Fluids* **131**, 45 (2016).
- [43] Y. Feng, P. Boivin, J. Jacob, and P. Sagaut, Hybrid recursive regularized thermal lattice Boltzmann model for high subsonic compressible flows, *J. Comput. Phys.* **394**, 82 (2019).
- [44] S. Guo, Y. Feng, and P. Sagaut, Improved standard thermal lattice Boltzmann model with hybrid recursive regularization for compressible laminar and turbulent flows, *Phys. Fluids* **32**, 126108 (2020).
- [45] F. Renard, Y. Feng, J.-F. Boussuge, and P. Sagaut, Improved compressible hybrid lattice Boltzmann method on standard lattice for subsonic and supersonic flows, *Comput. Fluids* **219**, 104867 (2021).
- [46] S. A. Hosseini, C. Coreixas, N. Darabiha, and D. Thévenin, Extensive analysis of the lattice Boltzmann method on shifted stencils, *Phys. Rev. E* **100**, 063301 (2019).
- [47] N. Frapolli, S. S. Chikatamarla, and I. V. Karlin, Lattice kinetic theory in a comoving Galilean reference frame, *Phys. Rev. Lett.* **117**, 010604 (2016).
- [48] B. Dorschner, F. Bösch, and I. V. Karlin, Particles on demand for kinetic theory, *Phys. Rev. Lett.* **121**, 130602 (2018).
- [49] E. Reyhanian, B. Dorschner, and I. V. Karlin, Thermokinetic lattice Boltzmann model of nonideal fluids, *Phys. Rev. E* **102**, 020103(R) (2020).
- [50] E. Reyhanian, B. Dorschner, and I. Karlin, Kinetic simulations of compressible non-ideal fluids: From supercritical flows to phase-change and exotic behavior, *Computation* **9**, 13 (2021).
- [51] E. Reyhanian, Thermokinetic model for compressible generic fluids, Ph.D. thesis, ETH Zürich, 2021.
- [52] N. Sawant, B. Dorschner, and I. V. Karlin, Detonation modeling with the particles on demand method, *AIP Adv.* **12**, 075107 (2022).
- [53] N. G. Kallikounis, B. Dorschner, and I. V. Karlin, Multiscale semi-Lagrangian lattice Boltzmann method, *Phys. Rev. E* **103**, 063305 (2021).
- [54] E. Zipunova, A. Perepelkina, A. Zakirov, and S. Khilkov, Regularization and the particles-on-demand method for the solution of the discrete Boltzmann equation, *J. Comput. Sci.* **53**, 101376 (2021).

- [55] E. Zipunova, A. Perepelkina, and A. Zakirov, Applicability of regularized particles-on-demand method to solve Riemann problem, *J. Phys.: Conf. Ser.* **1740**, 012024 (2021).
- [56] N. G. Kallikounis, B. Dorschner, and I. V. Karlin, Particles on demand for flows with strong discontinuities, *Phys. Rev. E* **106**, 015301 (2022).
- [57] Z. Guo, K. Xu, and R. Wang, Discrete unified gas kinetic scheme for all Knudsen number flows: Low-speed isothermal case, *Phys. Rev. E* **88**, 033305 (2013).
- [58] Z. Guo, R. Wang, and K. Xu, Discrete unified gas kinetic scheme for all Knudsen number flows. II. thermal compressible case, *Phys. Rev. E* **91**, 033313 (2015).
- [59] Z. Guo and K. Xu, Progress of discrete unified gas-kinetic scheme for multiscale flows, *Adv. Aerodyn.* **3**, 6 (2021).
- [60] B. T. Nadiga, An Euler solver based on locally adaptive discrete velocities, *J. Stat. Phys.* **81**, 129 (1995).
- [61] C. Sun, Lattice-Boltzmann models for high speed flows, *Phys. Rev. E* **58**, 7283 (1998).
- [62] P. Kauf, Multi-scale approximation models for the Boltzmann equation, Ph.D. thesis, ETH Zürich, 2011.
- [63] E. Reyhanian, Multiscale analysis of the particles on demand kinetic model, *Phys. Rev. E* **106**, 015304 (2022).
- [64] J. Meng, Y. Zhang, and X. Shan, Multiscale lattice Boltzmann approach to modeling gas flows, *Phys. Rev. E* **83**, 046701 (2011).
- [65] V. A. Rykov, A model kinetic equation for a gas with rotational degrees of freedom, *Fluid Dyn.* **10**, 959 (1975).
- [66] X. Nie, X. Shan, and H. Chen, Thermal lattice Boltzmann model for gases with internal degrees of freedom, *Phys. Rev. E* **77**, 035701(R) (2008).
- [67] S. Ansumali, S. Arcidiacono, S. S. Chikatamarla, N. I. Prasianakis, A. N. Gorban, and I. V. Karlin, Quasi-equilibrium lattice Boltzmann method, *Eur. Phys. J. B* **56**, 135 (2007).
- [68] X. He, X. Shan, and G. D. Doolen, Discrete Boltzmann equation model for nonideal gases, *Phys. Rev. E* **57**, R13(R) (1998).
- [69] B. Van Leer, Towards the ultimate conservative difference scheme. IV. A new approach to numerical convection, *J. Comput. Phys.* **23**, 276 (1977).
- [70] P. L. Roe, Characteristic-based schemes for the Euler equations, *Annu. Rev. Fluid Mech.* **18**, 337 (1986).
- [71] B. van Leer, Towards the ultimate conservative difference scheme. V. A second-order sequel to Godunov's method, *J. Comput. Phys.* **32**, 101 (1979).
- [72] G. Strang, On the construction and comparison of difference schemes, *SIAM J. Numer. Anal.* **5**, 506 (1968).
- [73] A. Tiwari and S. P. Vanka, A ghost fluid lattice Boltzmann method for complex geometries, *Int. J. Numer. Methods Fluids* **69**, 481 (2012).
- [74] Z. Guo and C. Shu, *Lattice Boltzmann Method and Its Applications in Engineering* (World Scientific, 2013); <https://www.worldscientific.com/doi/pdf/10.1142/8806>.
- [75] P. D. Lax, Weak solutions of nonlinear hyperbolic equations and their numerical computation, *Commun. Pure Appl. Math.* **7**, 159 (1954).
- [76] Z. Yang, C. Zhong, C. Zhuo, and S. Liu, Spatio-temporal error coupling and competition in meso-flux construction of discrete unified gas-kinetic scheme, *Comput. Fluids* **244**, 105537 (2022).
- [77] E. Toro and M. Vázquez-Cendón, Flux splitting schemes for the Euler equations, *Comput. Fluids* **70**, 1 (2012).
- [78] R. Loubère and M. J. Shashkov, A subcell remapping method on staggered polygonal grids for arbitrary-Lagrangian-Eulerian methods, *J. Comput. Phys.* **209**, 105 (2005).
- [79] P. D. Lax and X.-D. Liu, Solution of two-dimensional Riemann problems of gas dynamics by positive schemes, *SIAM J. Sci. Comput.* **19**, 319 (1998).
- [80] A. Kurganov and E. Tadmor, Solution of two-dimensional Riemann problems for gas dynamics without Riemann problem solvers, *Numer. Methods Partial Differ. Equ.* **18**, 584 (2002).
- [81] P. Woodward and P. Colella, The numerical simulation of two-dimensional fluid flow with strong shocks, *J. Comput. Phys.* **54**, 115 (1984).
- [82] V. Daru and C. Tenaud, Evaluation of TVD high resolution schemes for unsteady viscous shocked flows, *Comput. Fluids* **30**, 89 (2000).
- [83] G. Zhou, K. Xu, and F. Liu, Grid-converged solution and analysis of the unsteady viscous flow in a two-dimensional shock tube, *Phys. Fluids* **30**, 016102 (2018).
- [84] C. Cercignani, *Theory and Application of the Boltzmann Equation* (Scottish Academic Press, Edinburgh, 1975).
- [85] John D. Anderson, *Modern Compressible Flow: With Historical Perspective* (McGraw-Hill, 1990).
- [86] T. Ohwada, Structure of normal shock waves: Direct numerical analysis of the Boltzmann equation for hard-sphere molecules, *Phys. Fluids A* **5**, 217 (1993).
- [87] S. Ansumali, I. V. Karlin, S. Arcidiacono, A. Abbas, and N. I. Prasianakis, Hydrodynamics beyond Navier-Stokes: Exact solution to the lattice Boltzmann hierarchy, *Phys. Rev. Lett.* **98**, 124502 (2007).
- [88] H. Struchtrup, *Macroscopic Transport Equations for Rarefied Gas Flows* (Springer, Berlin, Heidelberg, 2005).
- [89] C.-W. Shu and S. Osher, Efficient implementation of essentially non-oscillatory shock-capturing schemes, II, *J. Comput. Phys.* **83**, 32 (1989).
- [90] Finite-difference hyperbolic-parabolic PDE solver on cartesian grids, <http://hypar.github.io/>.
- [91] G. Bird, *Molecular Gas Dynamics and the Direct Simulation of Gas Flows*, The Oxford Engineering Science Series (Clarendon Press, 1994).
- [92] J. Meng and Y. Zhang, Gauss-Hermite quadratures and accuracy of lattice Boltzmann models for nonequilibrium gas flows, *Phys. Rev. E* **83**, 036704 (2011).
- [93] E. Reyhanian, B. Dorschner, and I. Karlin, Exploring shock-capturing schemes for particles on demand simulation of compressible flows, *Comput. Fluids* **263**, 105947 (2023).